

NATL INST. OF STAND & TECH



A11106 977807



NIST  
PUBLICATIONS

**National Institute of Standards and Technology**  
Technology Administration, U.S. Department of Commerce

***NIST Technical Note 1544***

# **TEM Horn Antenna Design Principles**

Chriss A. Grosvenor  
Robert T. Johnk  
David R. Novotny  
Seturnino Canales  
Benjamin Davis  
Jason Veneman

QC  
100  
U5753  
#1544  
2007  
C.2



## **NIST Technical Note 1544**

# **TEM Horn Antenna Design Principles**

Chriss A. Grosvenor  
Robert T. Johnk  
David R. Novotny  
Seturnino Canales  
Benjamin Davis  
Jason Veneman

Electromagnetics Division  
National Institute of Standards and Technology  
325 Broadway  
Boulder, CO 80305

January 2007



**U.S. Department of Commerce**  
*Carlos M. Gutierrez, Secretary*

**Technology Administration**  
*Robert C. Cresanti, Under Secretary of Commerce for Technology*

**National Institute of Standards and Technology**  
*William A. Jeffrey, Director*

Certain commercial entities, equipment, or materials may be identified in this document in order to describe an experimental procedure or concept adequately. Such identification is not intended to imply recommendation or endorsement by the National Institute of Standards and Technology, nor is it intended to imply that the entities, materials, or equipment are necessarily the best available for the purpose.

**National Institute of Standards and Technology Technical Note 1544**  
**Natl. Inst. Stand. Technol. Tech. Note 1544, 74 pages (January 2007)**  
**CODEN: NTNOEF**

U.S. Government Printing Office  
Washington: 2007

---

For sale by the Superintendent of Documents, U.S. Government Printing Office  
Internet bookstore: gpo.gov Phone: 202-512-1800 Fax: 202-512-2250  
Mail: Stop SSOP, Washington, DC 20402-0001

# Contents

1. Introduction and Background . . . . .	1
2. TEM Horn Antenna Design . . . . .	2
2.1 Basic TEM Horn Antenna Design Principles . . . . .	4
2.1.1 TEM Horn Antenna Properties . . . . .	4
2.1.2 TEM Horn Characteristics . . . . .	6
2.2 1.2 m TEM Horn Antenna Design . . . . .	8
2.2.1 Balun for the 1.2 m TEM Horn Antenna . . . . .	9
2.2.2 1.2 m TEM Resistive Taper Design . . . . .	11
2.3 36 cm TEM Full-Horn Antenna with Ground Plane . . . . .	16
2.3.1 36 cm TEM Full-Horn Antenna Balun . . . . .	16
2.4 36 cm TEM Half-Horn Antenna . . . . .	20
2.4.1 36 cm TEM Half-Horn Antenna Feed-Point for Impedance Matching	22
2.4.2 36 cm TEM Horn Antenna – Cloth Resistive Taper . . . . .	23
2.5 Horn-to-Horn Responses and Measured Antenna Factors . . . . .	29
3. Antenna Numerical Design . . . . .	31
3.1 Numerically Modeled and Measured 1.2 m TEM Horn Antenna Patterns .	31
3.2 36 cm TEM Full-Horn Numerical Modeling . . . . .	36
3.3 TEM Half-Horn Numerical Design . . . . .	44
4. TEM Horn Antenna Applications . . . . .	53
4.1 Building-Material Measurements by Use of TEM Horn Antennas . . . . .	53
4.2 Aircraft Measurements . . . . .	59
4.3 RF Absorber Measurements . . . . .	63
4.4 Shelter Evaluations . . . . .	65
4.5 EMC Compliance Chamber Testing . . . . .	67
4.6 Conducted and Radiated UWB Emissions . . . . .	70
5. Conclusions . . . . .	70
6. Acknowledgments . . . . .	70
7. References . . . . .	71



# TEM Horn Antenna Design Principles

Chriss A. Grosvenor, Robert T. Johnk, David R. Novotny, Seturnino Canales, Benjamin Davis, and Jason Veneman

Electromagnetics Division  
National Institute of Standards and Technology  
325 Broadway, Boulder, CO 80305

*The National Institute of Standards and Technology has developed several ultrawideband, TEM horn antennas with phase linearity, short impulse duration, and a near-constant antenna factor. They are used as time-domain antennas for measuring impulsive fields with minimal distortion. The listed characteristics make TEM horn antennas ideal for separating events in the time domain. This time-domain separation allows for an accurate response from nearby scattering objects or representation of complicated antenna patterns or frequency responses from sources. This report describes the development of each antenna, their characteristics, plus numerical modeling applied to each antenna to study various aspects of design, and various measurement applications of these antennas. Applications include site attenuation measurements, chamber evaluations, radar imaging studies, and aircraft shielding evaluations. This report is intended for those who wish to construct these types of broadband antennas or to use the technology developed at NIST.*

*Key words:* antennas; antenna design; antenna measurements; numerical modeling; TEM horn antennas

## 1. Introduction and Background

Certain antennas on the market today are used for electromagnetic compatibility measurements such as radiated immunity and emissions testing. These are designed to cover a broad frequency spectrum while maintaining specified directional properties. However, trying to meet both criteria leads to distortion either in the phase or amplitude properties of the incoming signal. Designing an antenna with desired qualities in the time-domain will translate to an antenna with a broadband response in the frequency domain. A well-designed time-domain antenna should accurately reproduce the time waveform of the incoming field, thus preserving the amplitude and phase of the incoming signal [1- 4]. To provide desirable time-domain fidelity, an antenna must have both a constant amplitude response and a linear phase response in the frequency domain. Applications for which this characteristic is important include electromagnetic compatibility (EMC) facility evaluations [5], site attenuation measurements to determine ambient loss [6], room imaging studies [7] and shielding effectiveness studies on aircraft [8, 9].

The National Institute of Standards and Technology (NIST) has been designing transverse electromagnetic (TEM) horn antennas for over 30 years [10]. Desirable design

characteristics of time-domain TEM horn antennas include constant amplitude, linear phase, and high sensitivity to fields in both the time and frequency domains. The TEM horn antenna is designed to introduce minimal waveform distortion by allowing the fields within the structure to remain in the dominant transverse electromagnetic mode. By designing these antennas specifically for use with impulsive time-domain signals and having a broad frequency spectrum, time-domain distortion can be minimized [11, 12].

This technical report will discuss the design, construction, measurement and application of several TEM horn antennas. Four sections describe in detail three TEM horn antennas currently used by NIST: (1) a 1.2 m length TEM full-horn antenna, (2) a 36 cm TEM full-horn antenna, and (3) a 36 cm TEM half-horn antenna. The physical dimensions of the antenna, the impedance matching into and out of the antenna structure, and the design equations will be discussed in Section 2. Section 3 discusses the various uses of numerical-design packages, specifically, the finite-element method, to better understand the patterns and behavior of the electromagnetic fields associated with these antennas. The effect of finite ground-plane dimensions on the pattern is described. Section 4 addresses various applications of our antennas in field-test situations.

## 2. TEM Horn Antenna Design

A TEM horn antenna provides minimum-duration response to impulsive input or output fields and is able to discriminate between events occurring in the time domain. This is done by limiting the amount of propagation modeing in the antenna and by having a good impedance match design both at the feed-point to the antenna and at the aperture of the antenna. Inside the antenna, the fields should remain in the dominant mode, which for our antenna is the TEM mode. In other antennas, such as the log-periodic antenna, the spiral antenna, or the pyramidal horn antenna, phase dispersion occurs as the wave propagates along each of the elements, resulting in a greatly extended antenna response time to the fields. This is shown in the time-domain plot of Figures 1 and 2. Figure 1 shows the impulse response of the TEM horn antenna to the input waveform of an impulse generator for a waveform having a pulse width of approximately 300 ps. The TEM horn response time is on the order of a few nanoseconds. We can see that the TEM-horn antenna can accurately reproduce the incoming response of the surrounding environment and can resolve scattering events on the order of approximately 5 ns. The impulse response of a log-periodic antenna is shown in Figure 2, and is on the order of 40 ns. In this case, if we were trying to

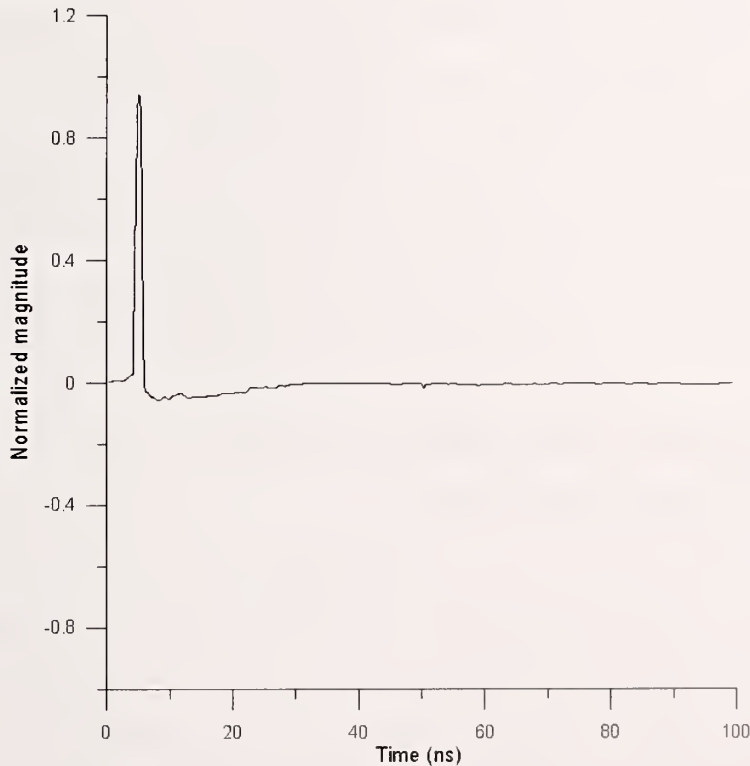


Figure 1. Time-domain response of TEM horn antenna to an applied impulsive electric field (private communication, Arthur Ondrejka.).

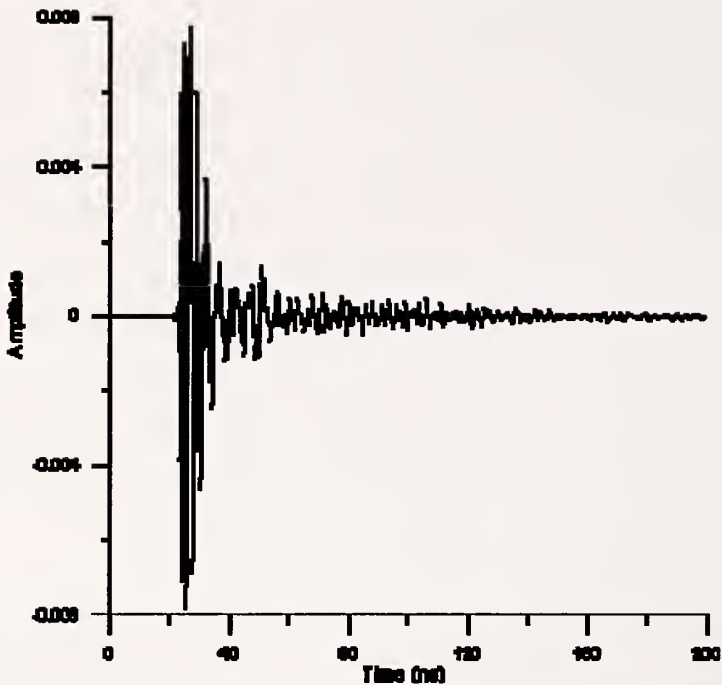


Figure 2. Time-domain response of log-periodic antenna to an impulsive electric field (private communication, Arthur Ondrejka.).

localize two events that are 10 ns apart, say reflections from the walls of a chamber, then the TEM horn antenna can discriminate between these events, but the log-periodic antenna cannot. The linear phase response of a TEM horn occurs because the antenna elements maintain the proper field and current relationships, by means of correct width and height ratios. This constant-impedance property is a key design criterion for TEM horn antennas. In order to illustrate the linear-phase property, we measured the transmission for two 1.2 m TEM horn antennas at various separation distances and plotted the unwrapped linear phase as shown in Figures 3 and 4. Figure 3 is the unwrapped phase response over the useable bandwidth of the antenna, and Figure 4 is the unwrapped phase response over a smaller frequency bandwidth shown to reveal detail.

## ***2.1 Basic TEM Horn Antenna Design Principles***

### ***2.1.1 TEM Horn Antenna Properties***

Figure 5 shows a general drawing of a TEM horn antenna [13, 14]. The width  $w$  and height  $h$  determine the impedance of the antenna, and a constant  $w/h$  ratio maintains constant impedance. The balun is used to convert input unbalanced electrical signals to balanced electrical signals in the antenna, and the resistive taper is used to reduce reflections from the end of the TEM horn section. The following sections describe the design of each part of this antenna.

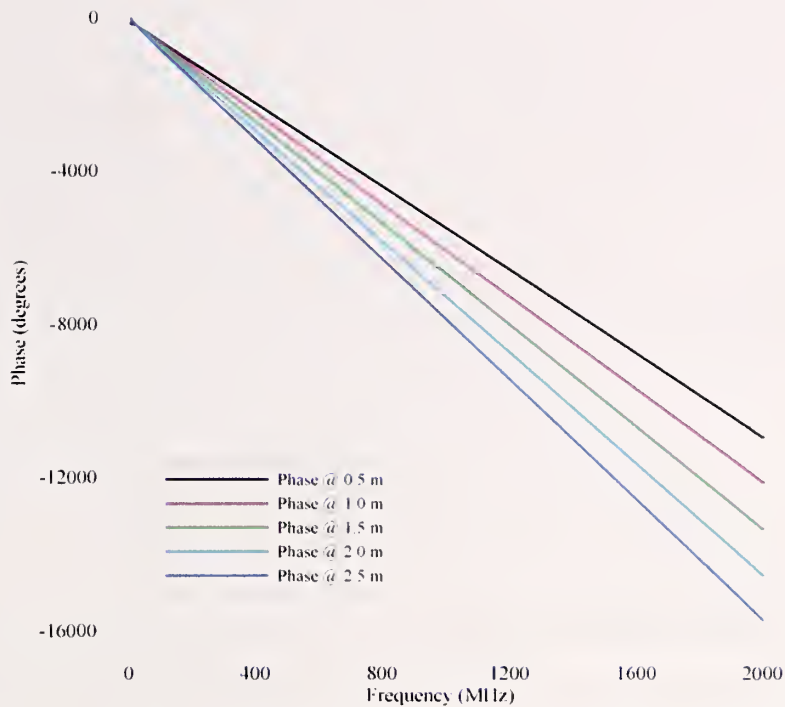


Figure 3. Unwrapped linear-phase response of 1.2 m TEM horn antenna over entire usable bandwidth and at various antenna separations.

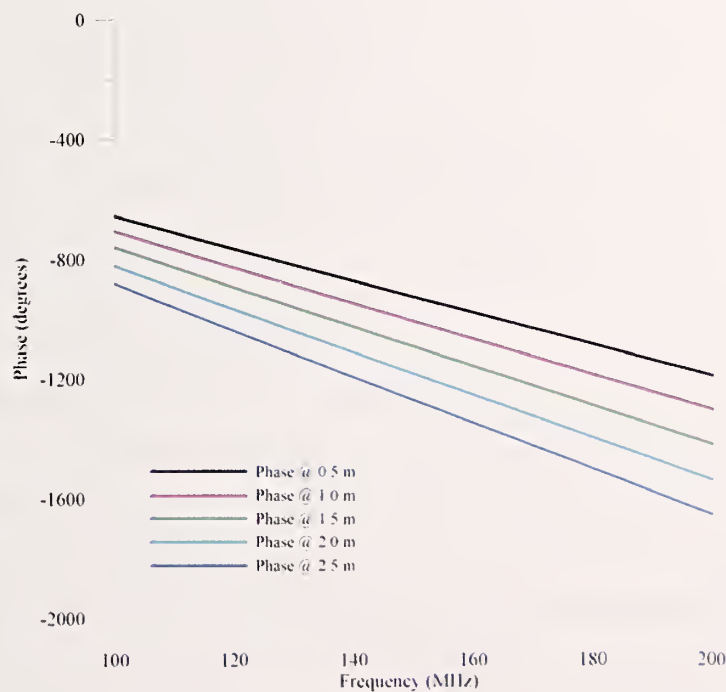


Figure 4. Unwrapped linear-phase response of 1.2 m TEM horn antenna over smaller frequency range and various antenna separations.

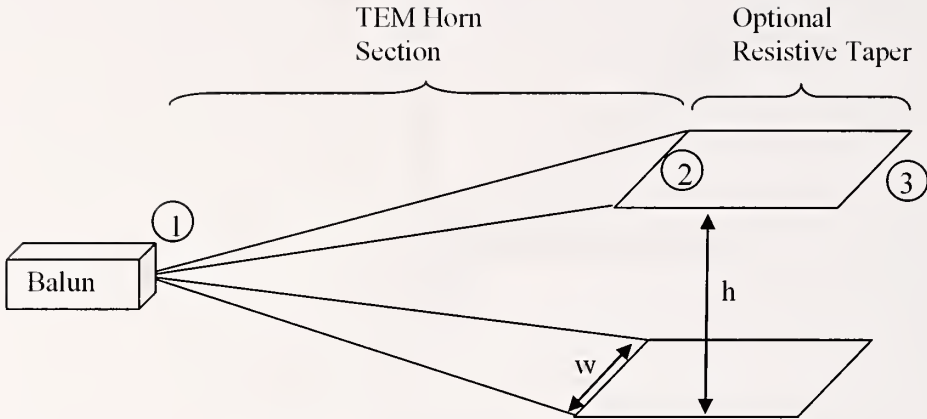


Figure 5. General design for TEM horn antenna.

### 2.1.2 TEM Horn Characteristics

In this subsection, we discuss how to design for phase linearity and constant amplitude and how to maximize bandwidth. As mentioned previously, the TEM horn antenna will show phase dispersion if the triangular elements (TEM horn Section, Figure 5) are not designed correctly. Triangular elements allow current path extremes along the structure, one directly down the center of the element, and the other along the edge. The edge path is obviously the longer, and currents on this path will be delayed. If the delay is large enough, the two signals will arrive at the output  $180^\circ$  out of phase, resulting in a strong reduction in output signal. This phase effect is easy to diagnose since it affects the amplitude response. Usually this will only be a problem only if the triangle is very wide across the aperture compared to its length. An equilateral triangle is as short as practical, but not recommended. Normally our antennas are several times longer than they are wide, and so this phase problem does not occur. Another reason why TEM horn antennas maintain good phase linearity is that the currents in the conductors are moving in the same direction as the electric fields. This is not true in the case of other antennas, such as dipole antennas [15, 16]. A short dipole also maintains linear phase response, but for a different reason; the currents in the structure, although perpendicular to the field, have only a short distance to flow, and therefore respond without delay to the input fields. However, a long dipole [17] does have a noticeable phase problem, because the currents require a significant time to flow down the dipole, and they flow in a direction perpendicular to that of the electric field. As a result, the impulse response of a long dipole is greatly extended, resembling a square wave, and having a repetition frequency equal to the resonant frequency of the dipole.

Three conditions must be satisfied for a TEM horn antenna to have constant-amplitude response (see Figure 5): (1) the impedance of the antenna/balun must be matched to that of the receiver, (2) the input impedance must be matched to the antenna's internal impedance, and (3) the input and output coupling of the antenna must minimize resonances and multiple reflections. The amplitude response or antenna factor gives us an indication of the sensitivity of an antenna's response to various frequencies across this bandwidth. Figure 6 shows the amplitude response for various antennas, including the 1.2 m TEM horn antenna developed by NIST. The antenna factor (AF) is given by

$$AF(dB) = 20 \cdot \log\left(\frac{E_{incident}}{V_{received}}\right), \quad (1)$$

where the electric field is typically measured at a distance of 1 m. Most of the antennas shown are sensitive to the fields over only a few hundred megahertz (MHz), but the TEM horn antenna factor is constant from approximately 30 MHz to 1500 MHz.

Research has shown that an input voltage standing wave ratio (VSWR) of less than 1.2 yields the best impedance match. The components of interest are the input coaxial cable, the balun, the antenna, and the resistive termination. The balun and the resistive termination will be

40 --

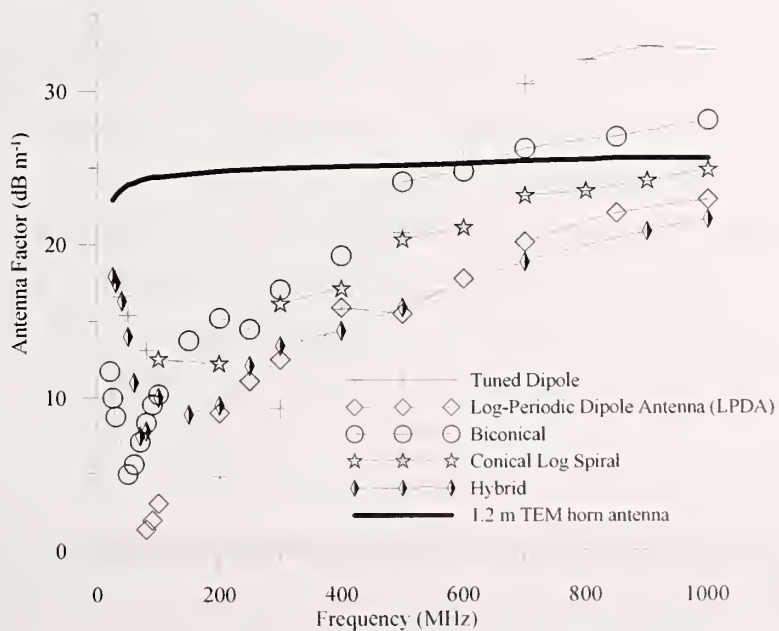


Figure 6. Antenna factors for various antenna types.  
(Data used with permission from ARA Technologies, Inc. [18])

discussed in later sections, but to achieve a constant antenna factor within the antenna, impedance must be held constant. The NIST TEM horn antennas are designed as parallel plate transmission lines, with a gradual, constant-impedance, tapered transition from the feed-point/coaxial air line at one end, to the aperture dimension of its output at the other end. The impedance of a parallel plate transmission line is a function of the ratio of the width  $w$  of the conductive elements to the spacing between the elements  $h$  (height). The width to height ratio,  $w/h$ , is kept constant by making the elements narrower in proportion to the decrease in spacing. This impedance can be calculated with the microstrip equations of Gardiol or Gupta [19 - 21]:

$$Z_0 = \frac{2}{\sqrt{\epsilon_r}} \cdot 59.95 \cdot \ln\left(\frac{8h}{w} + \frac{w}{4h}\right), \quad (2)$$

which is true for  $0 \leq w/h \leq 1$ , i.e., for antenna impedances greater than  $252 \Omega$ . The relative dielectric constant is equal to that of Styrofoam ( $\epsilon_r = 1.05$ ). For antennas with impedances between  $58.4 \Omega$  and  $252 \Omega$ , or  $1 < w/h \leq 10$ , we use the following equation:

$$Z_0 = \frac{2}{\sqrt{\epsilon_r}} \cdot \frac{376.69}{\left[\frac{w}{h} + 2.42 - 0.44 \cdot \frac{h}{w} + \left(1 - \left(\frac{h}{w}\right)^6\right)\right]}. \quad (3)$$

We used this equation to design an antenna with  $50 \Omega$  impedance, and it worked very well even though eq. (3) was not valid for this impedance value. We note that the equation, as given by Gardiol [20], is used to calculate the impedance of a microstrip transmission line, a driven conductor spaced over a ground plane. We use the fact that the driven element has an image in the ground plane, so that the antenna appears to be a microstrip line with a real conductor in place of the image and with the ground plane removed. This requires only two slight changes: the impedance of the antenna is twice that of the microstrip, and the spacing between the antenna elements is twice the microstrip height. This is the reason for the two extra factors of 2 above. The antenna has a low-frequency cut-off which is related to the length of the antenna, as determined experimentally.

## 2.2 1.2 m TEM Horn Antenna Design

Figure 7 shows a model of the TEM horn antenna, and Figure 8 shows an actual NIST-built 1.2 m TEM horn antenna. The dimensions of the antenna are  $w = 20$  cm,  $h = 24.5$  cm,  $L_h = 1.2$  m, and  $L_x = 41.5$  cm. Therefore, the impedance of the 1.2 m TEM horn antenna is  $194 \Omega$ , as given by eq. (3). The antenna is constructed with a 4:1 transformer/balun, two outer antenna

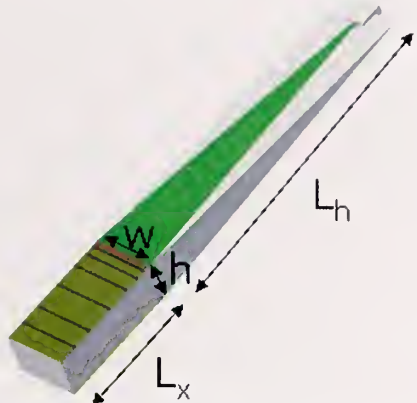


Figure 7. Numerical model of a 1.2 m TEM horn antenna.

plates without a ground plane and a resistively tapered section. The photograph in Figure 8 shows each section of the 1.2 m TEM horn antenna. From left to right we see the resistive termination, the antenna element section, the balun, and the coaxial airline surrounded by ferrite beads to suppress common-mode current. A close-up of this last section is shown in Figure 9. The Styrofoam between the elements is used as a support, and it has a relative permittivity of 1.05. It has little effect on the internal field structure, thus maintaining the proper VSWR and impedance.

### ***2.2.1 Balun for the 1.2 m TEM Horn Antenna***

We have used two types of RF pulse transformers or baluns in our 1.2 m TEM horn antennas. The first is rated from 500 kHz to 1 GHz and is configurable for either a  $50\ \Omega$  unbalanced or a  $200\ \Omega$  balanced transformer. It has a rise time of 0.18 ns and an insertion loss of approximately 0.4 dB. Figures 10 and 11 show the pin configuration and dimensions for this first balun. The second balun has a cleaner impulse response than the first, but is only rated from 2 MHz to 750 MHz. It can also be configured as either a  $50\ \Omega$  unbalanced or a  $200\ \Omega$  balanced transformer and the pin diagram is shown in Figure 12.



Figure 8. A NIST-developed 1.2 m TEM horn antenna.

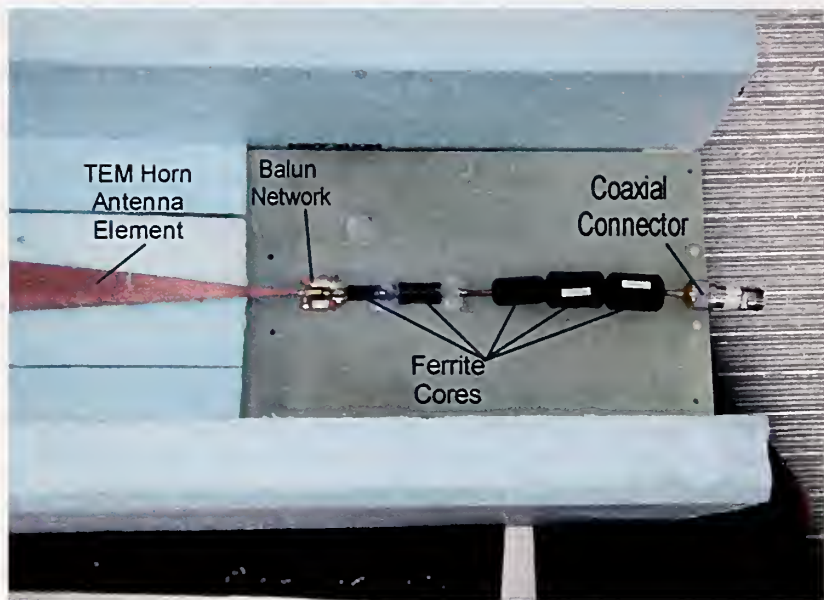


Figure 9. Close-up view of balun network, ferrite cores, and coaxial connector for a 1.2 m TEM horn antenna.

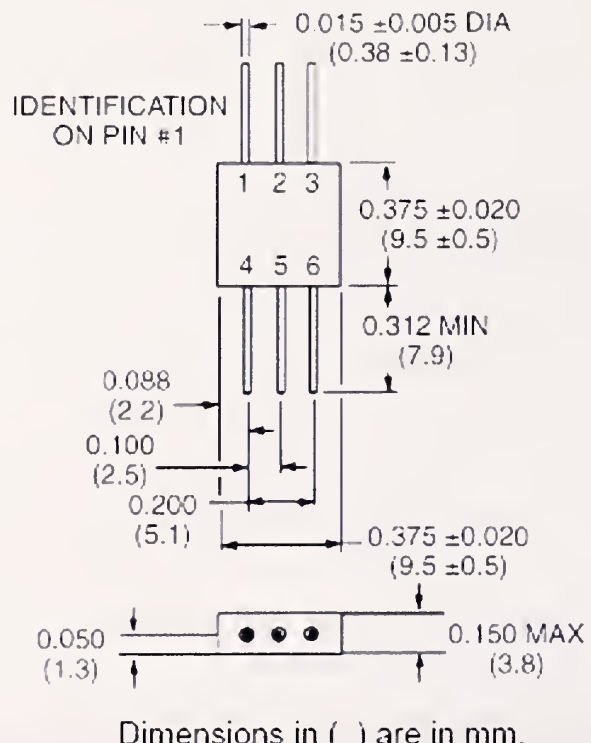


Figure 10. Pin diagram for balun 1 1.2 m TEM antenna.  
(Data used with permission from M/A COM, Inc. [22].)

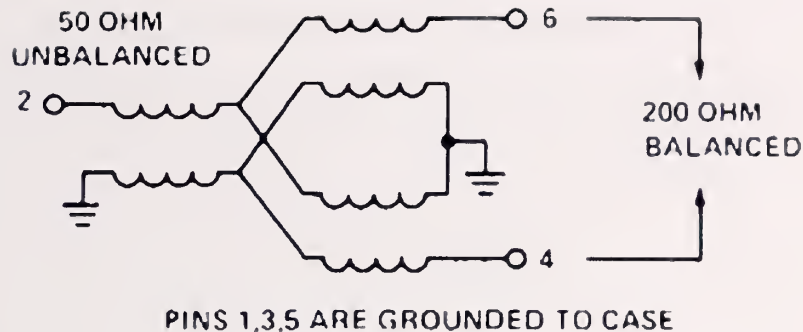


Figure 11. Balun 1 configuration for  $50 \Omega$  unbalanced operation.  
(Data used with permission from M/A COM, Inc. [22].)

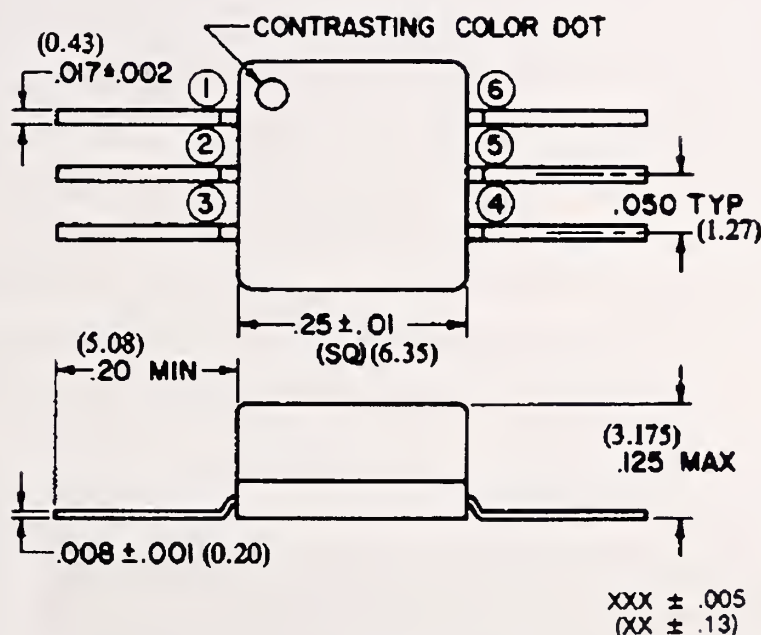


Figure 12. Pin diagram for balun 2: 1.2 m TEM antenna .  
(Data used with permission from Sirenza Microdevices, Inc. [23].)

### 2.2.2 1.2 m TEM Horn Resistive Taper Design

The resistive taper is designed and engineered to reduce reflections from the aperture of the antenna. Each TEM antenna has a unique design for the resistive taper, so each will be discussed in its respective section. Much design time has been spent determining the best way to provide an impedance transition from the parallel-plate impedance to free-space impedance. Several papers [24 - 26] describe how to resistively load antennas for the best impedance match. The ideal load distribution for a dipole antenna is an exponential distribution [4, 24]. Figure 13

illustrates the resistive taper for one of our 1.2 m TEM horn antennas. This particular taper was designed with chip resistors located at the junctions between copper sections. The exponential distribution is controlled by both the size of the resistors and the size and the distribution of the copper sections. The copper is a piece of single-side cladded material in which areas were etched away to provide gaps for placement of resistors. The etched centerline is used to control over-moding. Table 1 shows the gap width, section lengths, nominal resistor values, number of resistors at each junction, and total gap resistance currently used in our antennas. The loading of the resistive taper increases roughly exponentially with distance from the aperture of the antenna. Figure 14 is a schematic of this configuration. The slots are bridged by a row of resistors soldered to the conductors on either side of the slot. From 6 to 13 resistors are used, depending on the desired value of the resistance. The spacing between the slots should neither be the same, nor harmonically related. This may produce a resonance at the common spacing.

Likewise, maintaining any spacing greater than one-quarter wavelength at the highest frequency of use is not desirable. In order to maintain a reasonably uniform current distribution on the antenna, we recommend that the individual resistors be spaced less than  $0.1 \lambda$  apart for the highest operating frequency. Either ceramic chip or one-eighth-watt carbon resistors can be used below 1 GHz. Above 1 GHz, only ceramic chips should be used. Figures 15 and 16 show input impulse responses without and with a resistively loaded taper. The aperture causes a

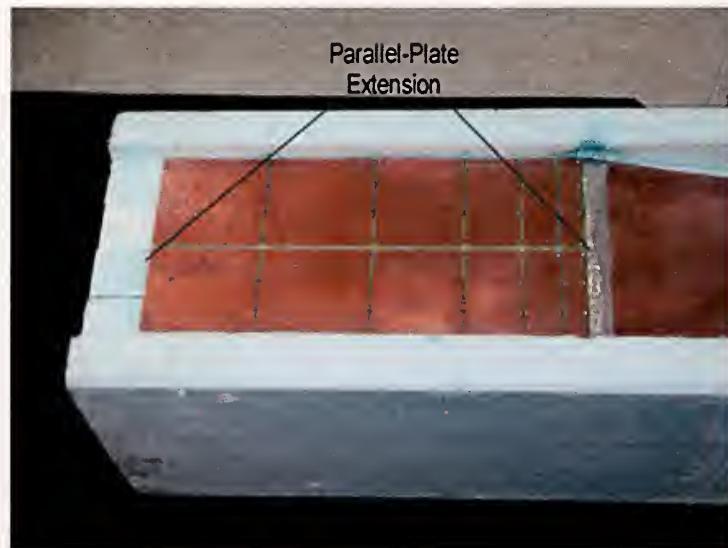


Figure 13. Resistively tapered aperture for 1.2 m TEM horn antenna.

**Table 1. Dimensions and resistor values for 1.2 m TEM resistive taper.**

Copper section length $l_i$ (mm)	Nominal resistor values ( $\Omega$ )	No. of resistors along gap	Total gap resistance, $z_i$ ( $\Omega$ )
19.1	9.4	11	0.85
31.8	15.95	13	1.23
50.6	22.9	11	2.08
82.5	38.6	7	5.51
101.6	62.5	8	7.81
104.8	93.9	6	15.65

fairly large reflection between 15 ns to 20 ns. When the aperture is resistively loaded, the reflection is reduced significantly. Figure 17 shows time-domain impulse responses of a pair of 1.2 m TEM horn antennas having different baluns and tapers. The first major reflection is from the balun/transformers, and the second train of reflections is from the resistive taper. Figure 18 is the time-gated, reflected frequency response of a pair of 1.2 m TEM horn antennas.

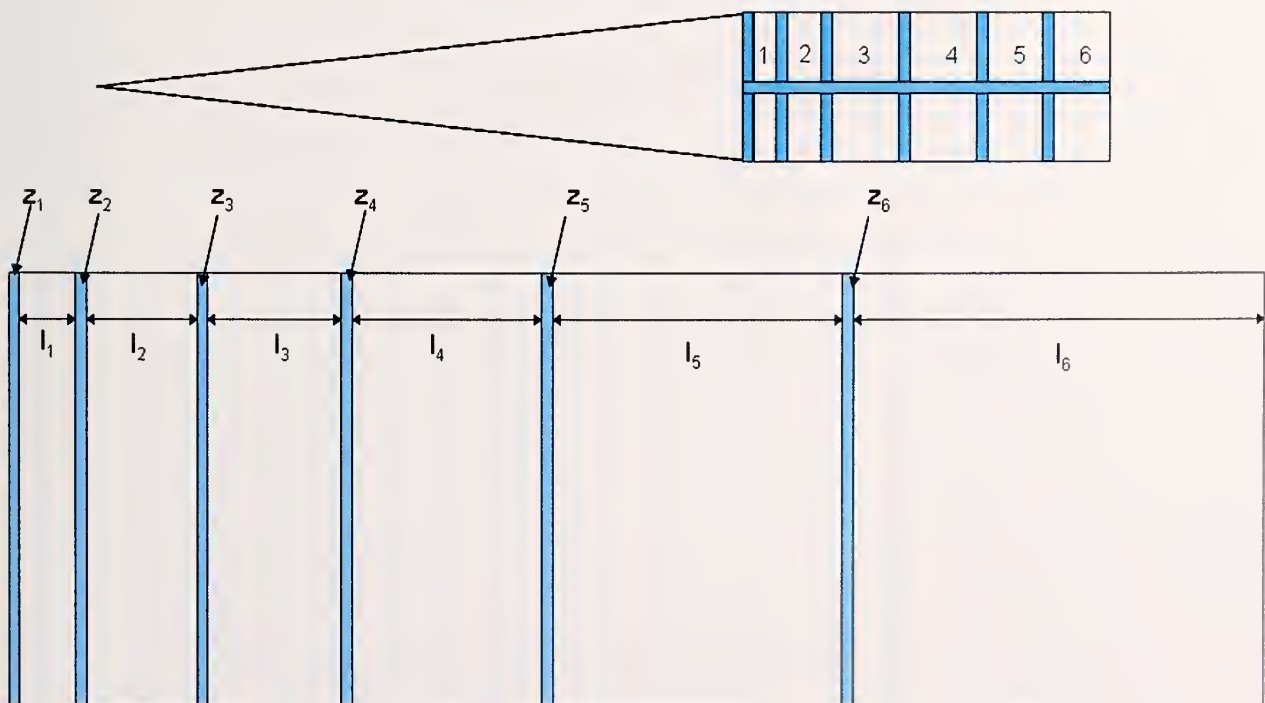


Figure 14. Resistively tapered section for 1.2 m TEM horn antenna.

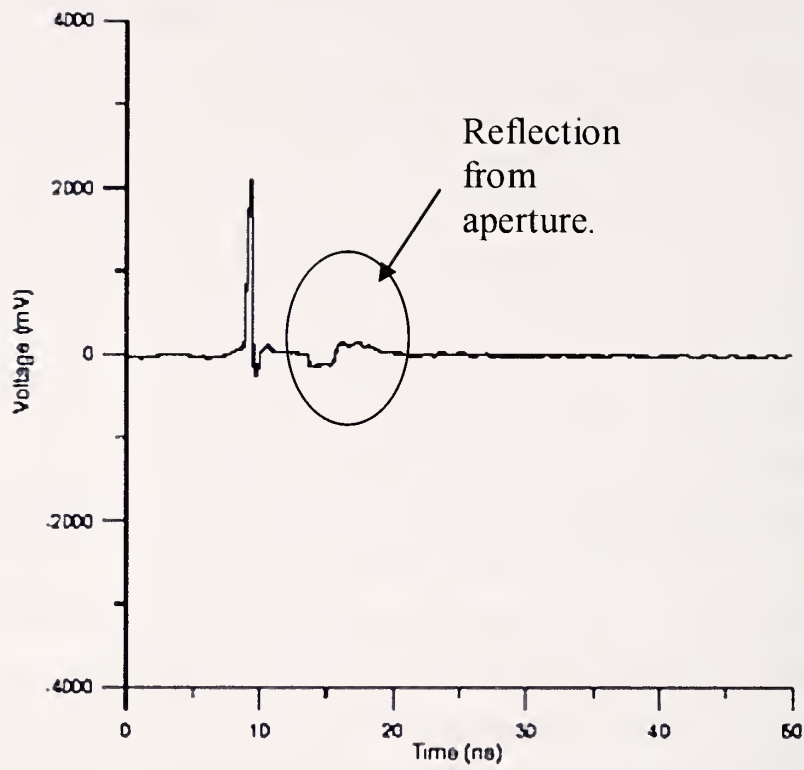


Figure 15. Input reflection characteristics of an unloaded TEM horn antenna.  
(Private communication with Arthur Ondrejka.)

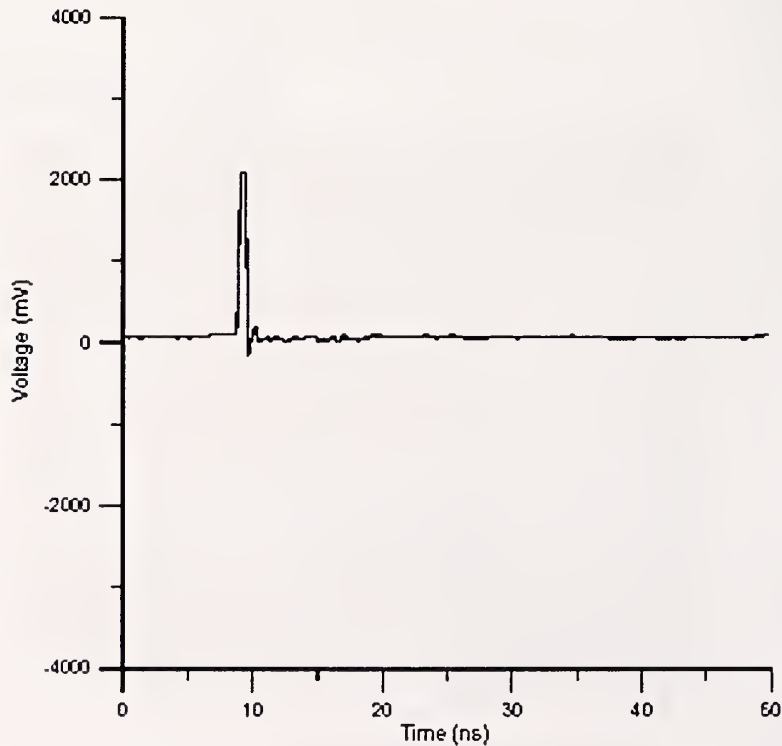


Figure 16. Input reflection characteristics of a resistively loaded TEM horn antenna.  
(Private communication with Arthur Ondrejka.)

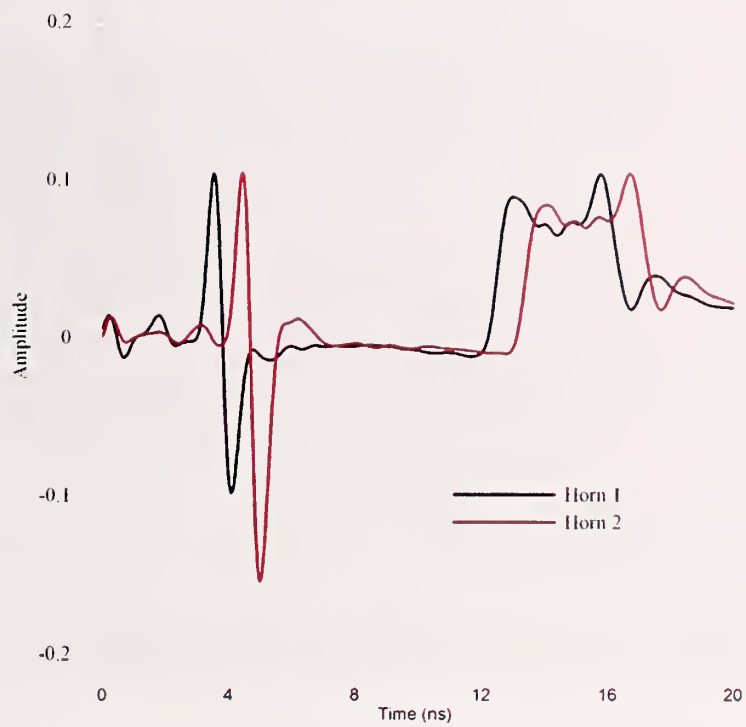


Figure 17. Time-domain impulse response of two 1.2 m TEM horn antennas having different baluns and tapers.

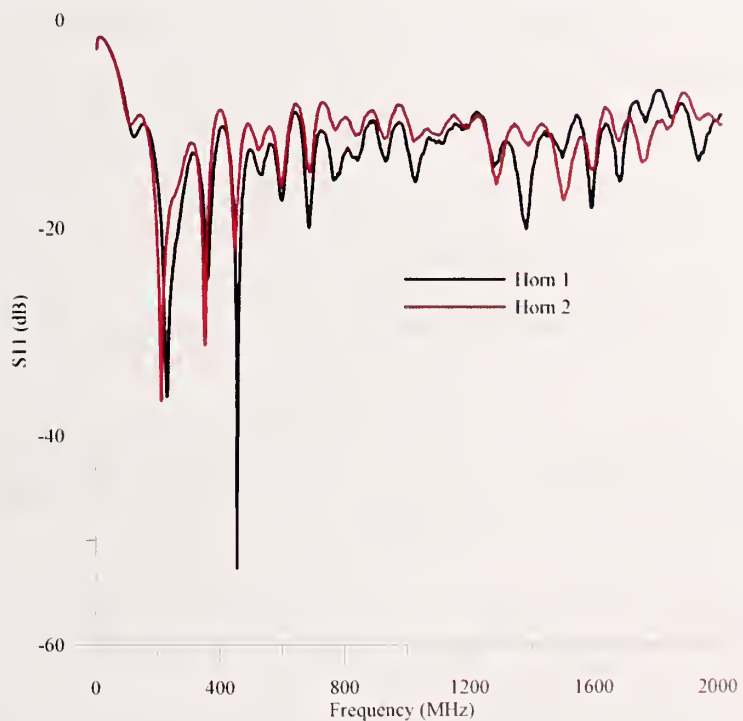


Figure 18. Frequency-domain input reflection coefficient of two 1.2 m TEM horn antennas having different baluns and tapers.

## 2.3 36 cm TEM Full-Horn Antenna with Ground Plane

Figure 19 shows a model of the original NIST TEM horn antenna, and Figure 20 shows the NIST-built 36 cm TEM horn antenna. The dimensions of the antenna are  $w = 23.3$  cm,  $h = 9.1$  cm,  $L_h = 36.6$  cm. This results in an antenna impedance of approximately  $95 \Omega$ . The antenna is constructed with two outer antenna plates and originally with a ground plane in between the elements. This was later removed, as discussed in the previous section and as is also discussed in the numerical modeling section below. The balun is a passive device that converts the unbalanced input current into two balanced currents that drive two  $50 \Omega$  coaxial transmission lines  $180^\circ$  out of phase. A close-up of this section is shown in Figure 21. Resistive tapers have not yet been implemented in this particular antenna; however, Section 2.4.2 describes a resistive taper design for a 36 cm TEM half-horn antenna that will eventually be implemented.

### 2.3.1 36 cm TEM Full-Horn Antenna Balun

The baluns are known as hybrid couplers/junctions. It is a passive design that allows an input signal to be converted to a combination of in-phase ( $0^\circ$ ) and an out-of-phase ( $180^\circ$ ) output signal, to provide a balanced antenna drive. We have also looked at balun designs in a microstrip environment [27, 28] but have not yet incorporated these.

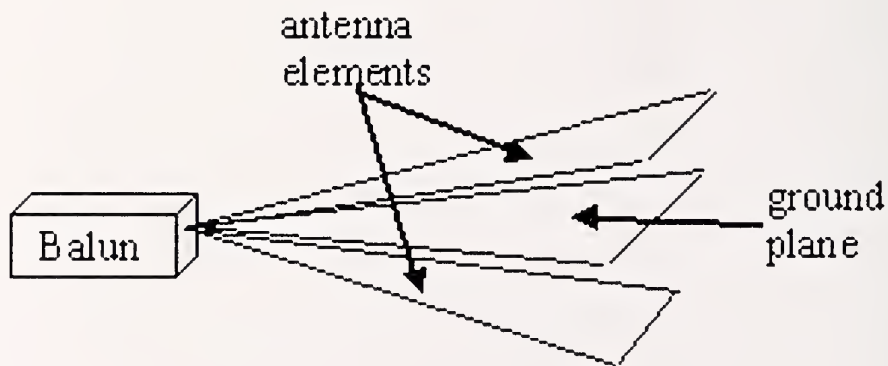


Figure 19. Diagram of a 36 cm TEM full-horn antenna with ground plane.



Figure 20. Photograph of 36 cm TEM full-horn antenna.

The antenna baluns were implemented by use of commercially available  $0^\circ$  to  $180^\circ$  microwave hybrid couplers. We measured the hybrid couplers of two separate manufacturers for use in the TEM horn antennas. The insertion loss and phase through the hybrid determines the one most suitable for our design. Figure 22 shows the insertion loss through both ports of Hybrid A. The insertion phase through the out-of-phase port for Hybrid A is shown in Figure 23. This plot shows that hybrid losses vary from about 1 dB at low frequencies to 5 dB at high frequencies. The insertion phase shows variations of less than a degree from 45 MHz to 2000 MHz and variations of about  $5^\circ$  at the upper frequencies. For Hybrid B, we see the same loss magnitudes through the hybrid (Figure 24), but the phase (Figure 25) seems to be linear across a larger frequency band, and therefore this is the hybrid used in our 36 cm TEM full-horn antennas.

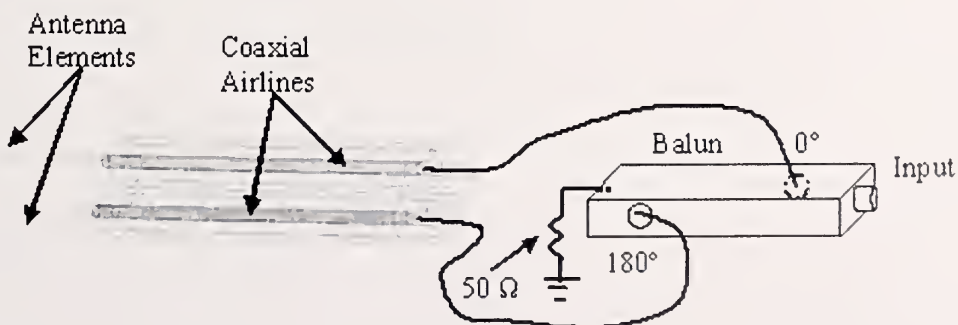


Figure 21. Two  $50 \Omega$  coaxial cables driven  $180^\circ$  out-of-phase.

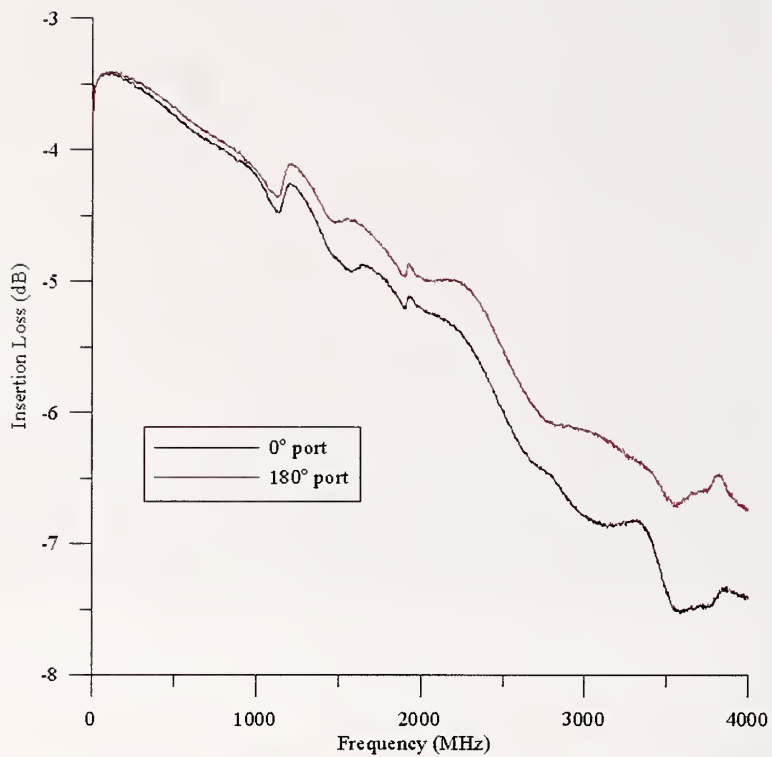


Figure 22. Insertion loss for Balun A through the  $0^\circ$  and  $180^\circ$  ports.

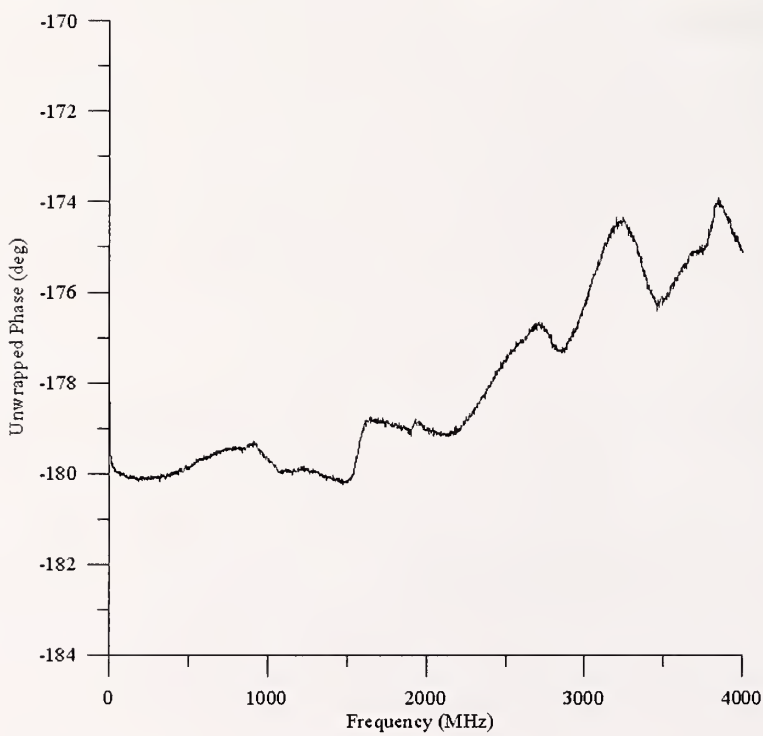


Figure 23. Insertion phase through Balun A.

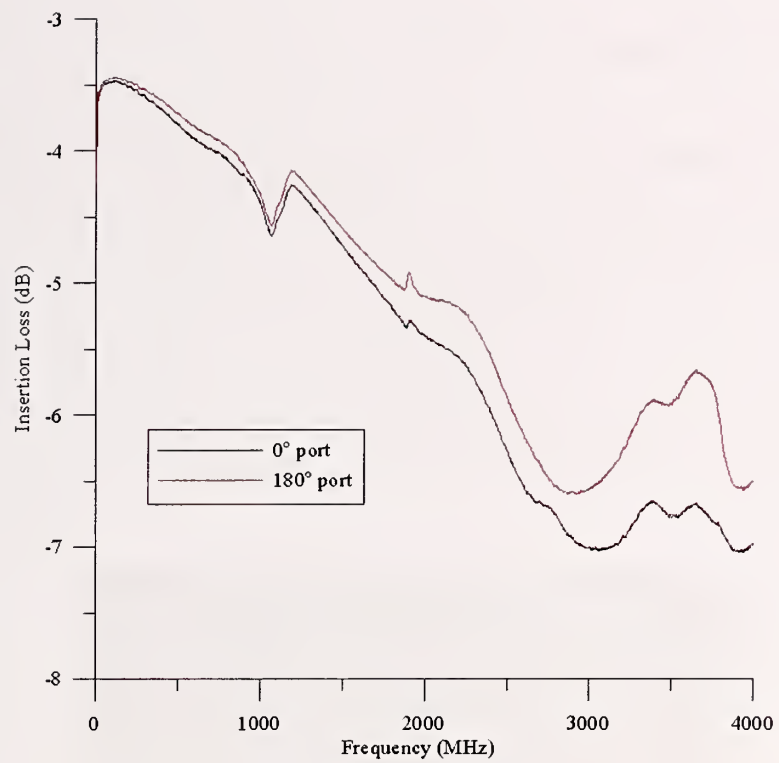


Figure 24. Insertion loss for Balun B through the  $0^\circ$  and  $180^\circ$  ports.

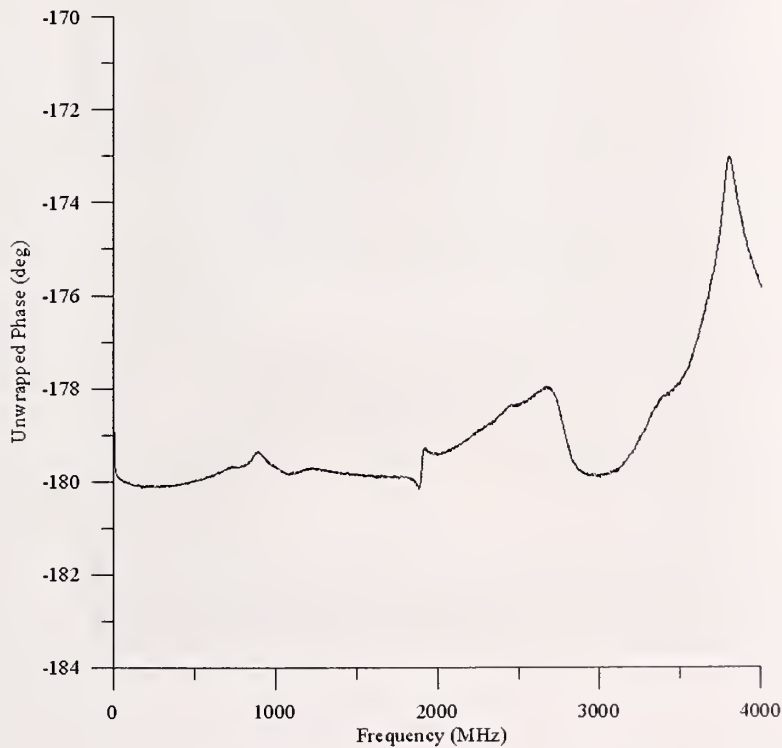


Figure 25. Insertion phase through Balun B.

## **2.4 36 cm TEM Half-Horn Antenna**

Figure 26 is a photograph (top view) of a 36 cm long TEM half-horn antenna. The dimensions of the antenna are  $w = 22.7$  cm,  $h = 3.9$  cm, and  $L_h = 36.5$  cm, and the angle formed between the ground plane and the antenna plate is  $6^\circ$ . The impedance of this antenna is approximately  $45 \Omega$ . This antenna is designed to be supported over a large ground plane. The ground plane removes the need for a balun. Figure 26 shows the main antenna element (triangular in shape), a copper ground plane to which the coaxial cable is attached, Styrofoam to provide support, and the cloth resistive taper. Drawings of this antenna are shown in Figures 27 to 29.



Figure 26. Top view of 36 cm TEM half-horn antenna

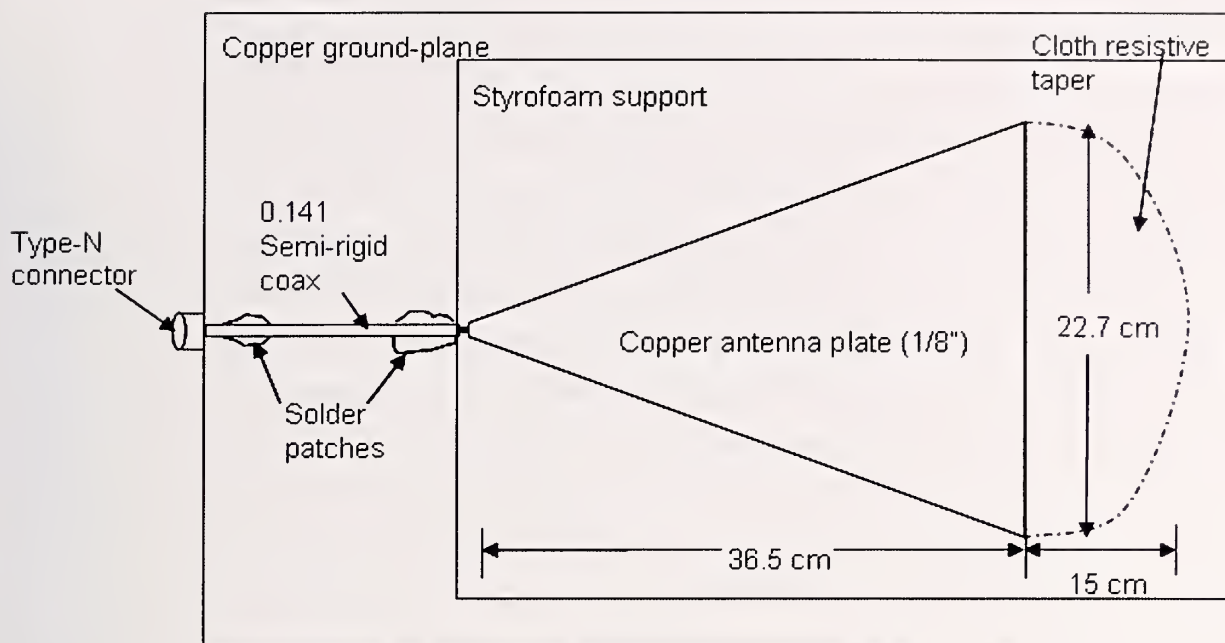


Figure 27. Top view drawing of 36 cm TEM half-horn antenna.

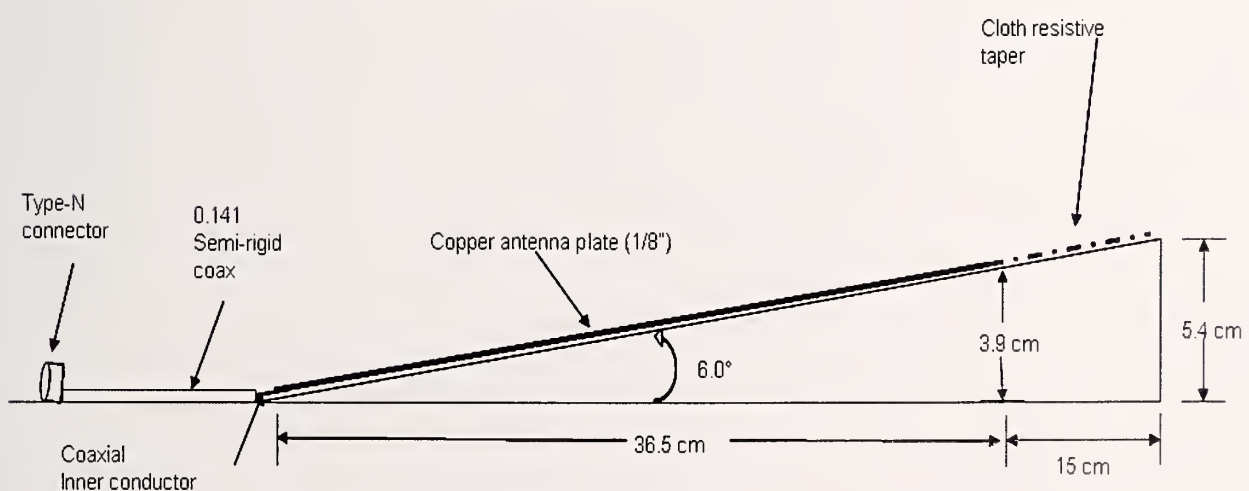


Figure 28. Side view drawing of 36 cm TEM half-horn antenna.

## 2.4.1 36 cm TEM Half-Horn Antenna Feed-Point for Impedance Matching

Figure 29 shows a close-up of the feed-point to the antenna. Although this feed-point construction is discussed in detail here, it applies to the feed-point of all TEM horn antennas. The first thing that one notices is that the antenna element does not come to a point. This is cut such that the width of the element at the feed-point and the height of the coaxial cable provide the appropriate impedance match to  $50 \Omega$ . The aspect ratio of the plates must be chosen to maintain a  $50 \Omega$  impedance at both the feed-point and the aperture. The second key feature is that the solder patch is at the very end of the coaxial cable. This minimizes the inductance between the ground plane and outer conductor of the coaxial feed cable. The capacitance depends on the distance between the outer conductor of the coax and the antenna plate, so the dielectric bead can touch the antenna plate but the outer coaxial cable cannot. This is a rather delicate connection, so care must be taken to secure the antenna element to the Styrofoam and ground plane.

## 2.4.2 36 cm TEM Horn Antenna – Cloth Resistive Taper

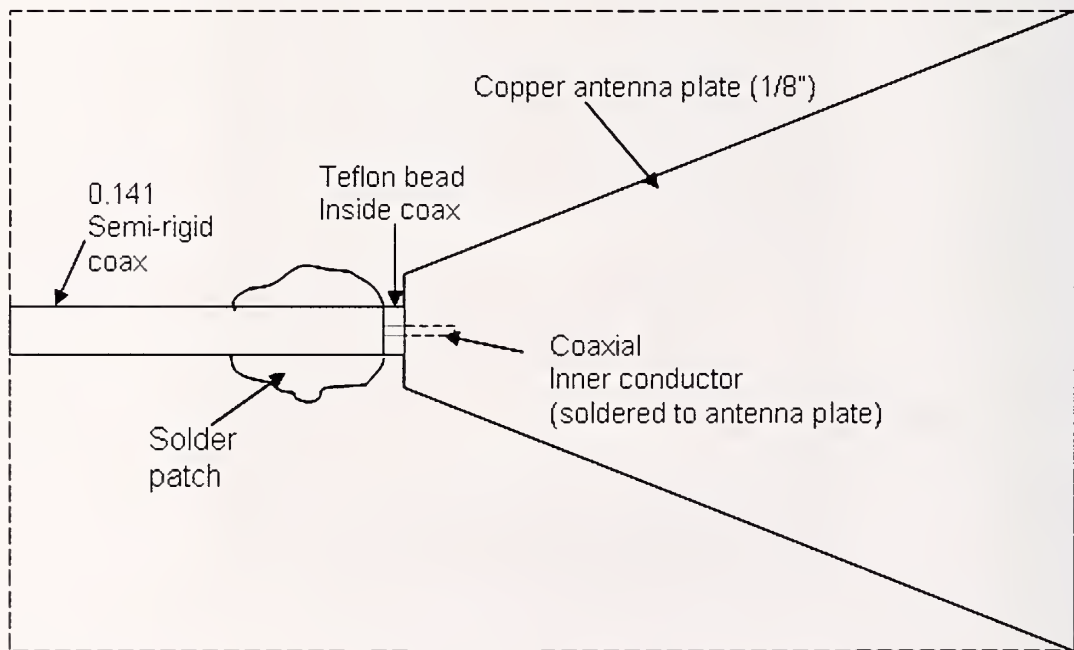


Figure 29. Close-up view of feed-point detail for the 36 cm TEM half-horn antenna.

In this section we will discuss the design of the resistive taper for the TEM half-horn antenna. The resistive taper is used to minimize the reflection at the aperture. Figure 30 shows the input reflection characteristics without a resistive taper. The first reflection is from the feed-point transition between the  $50 \Omega$  coaxial cable and the upper plate of the antenna. The second larger reflection is due to the aperture. As noted previously we can minimize the reflection from the feed-point by making sure the feed-point impedance is matched and the cabling has intimate contact with the ground plane. The aperture reflection can be minimized by providing a transition to  $377 \Omega$ . In the 1.2 m TEM horn antennas, this was accomplished using copper-clad circuit boards and adding resistors. In the course of research we found that this can also be accomplished by using various layers of resistive cloth between the aperture and free-space for the smaller TEM half-horn antennas.

We looked at several types of resistive cloth for use in the resistive taper design. The first was a

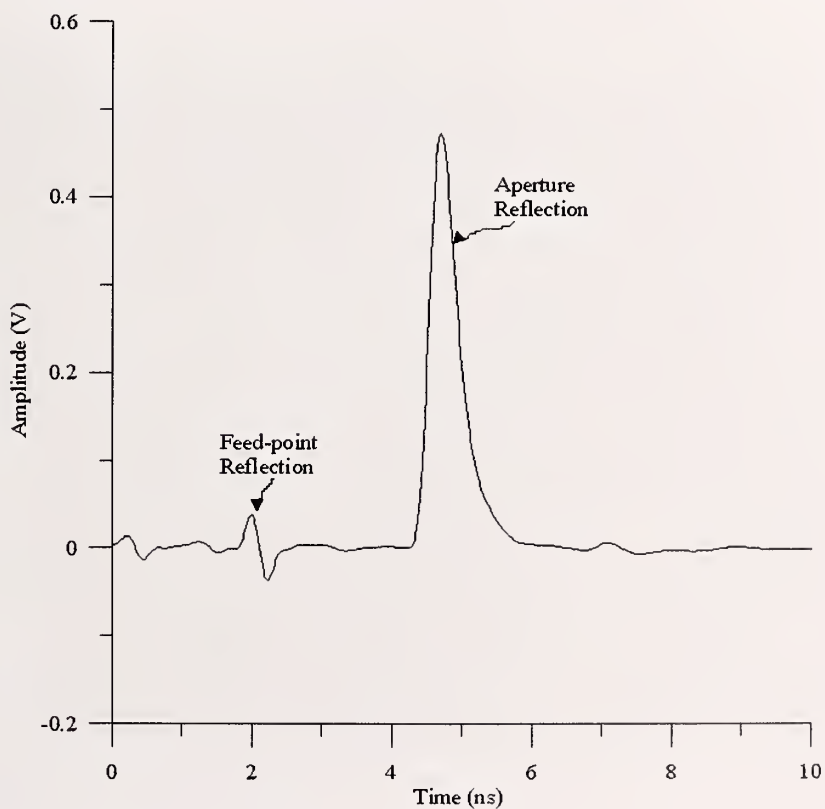


Figure 30. Time-domain plot of the reflections from the TEM half-horn antenna without a resistive taper.

stranded-copper cloth. It is a copper-coated fabric. The second material has a black-silvery sheen to it and was made with a carbon-loaded polymer on rayon threads. The third cloth had a lighter shading of black, due to less carbon loading. We measured the resistance of each sample with an ohmmeter, using a fixture to hold the fabric taut. The calculation of the sheet resistivity is summarized in the following table:

**Table 2. Various Resistive Fabric s and Their Measured Resistivity.**

Fabric (dimensions in cm)	Resistivity ( $\Omega \cdot \text{m}$ )
Copper-coated sample (11.4 x 5.4)	0.142
Dark black sample 1 (15 x 4.3) Measured along grain	259
Dark black sample 1 (15.4 x 4.2) Measured cross-grain	344
Light black sample 2 (15.3 x 4.1) Measured along grain	785
Light black sample 2 (14.9 x 4.3) Measured cross-grain	855

The sheet resistance  $R$  is given by

$$R = \rho \frac{L}{A}, \quad (4)$$

where  $\rho$  is the resistivity,  $L$  is the length of the sample, and  $A$  is its cross-sectional area, given by the product of width and thickness. We measured the resistance  $R$  with an ohmmeter and solved for the sheet resistance  $R_s$  or  $\rho/t$  ( $t$  is the thickness of the sample), so that our final equation becomes

$$\frac{\rho}{t} = R_s = \frac{Rw}{L}. \quad (5)$$

We considered how different materials could be used to minimize the reflection from the antenna aperture. The materials were arranged so that most of the fields would dissipate quickly, thereby minimizing aperture radiation. The copper material provides a low-impedance environment and the black fabric a high-impedance environment in which to dissipate the fields. Figure 31 shows a photograph of the first design, a copper sheet with triangular points, allowing the fields to dissipate quickly. This copper fabric was sewn to the black resistive cloth with conductive thread. This allows the remaining fields to dissipate in the black resistive fabric. The complete resistive taper section is 15 cm long, which is one-half wavelength at 500 MHz. This frequency was chosen to limit the length of the taper. The resistive taper was attached to the copper antenna plate with a conductive epoxy. The improvement to the aperture reflection characteristics are shown in Figure 32. We see that the aperture reflection was reduced by half by introducing the resistive taper.



Figure 31. Copper fabric for resistive taper backed by black resistive cloth.

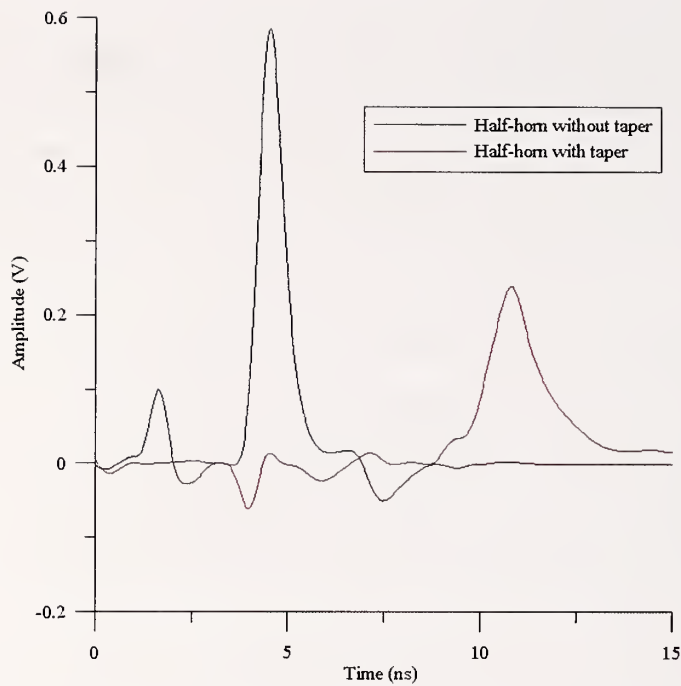


Figure 32. Plot showing the decrease in amplitude of the aperture reflection after resistive termination was incorporated.

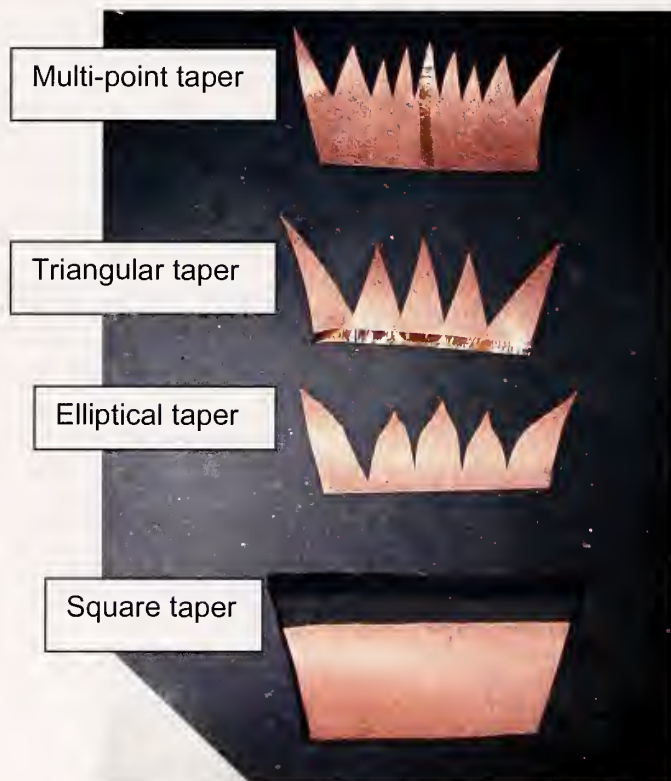


Figure 33. Various cloth resistive taper designs.

We experimented with some other tapered designs to see whether we could minimize the reflection further. These are shown in Figure 33. The reflection coefficient for each type of termination is shown in Figure 34. We can see that the “layered-moon” taper, shown in Figure 35, and the elliptical taper of Figure 33 have the lowest reflection coefficient across the measured frequency band. Figure 36 shows the input time-domain response of the best taper. This taper decreased the reflection from the aperture by almost half for two of our horns, Horn 1 and Horn 2. Thus we have shown that we can reduce the reflection at the end of a TEM half-horn antenna by using a fabricated resistive taper of conductive cloth.

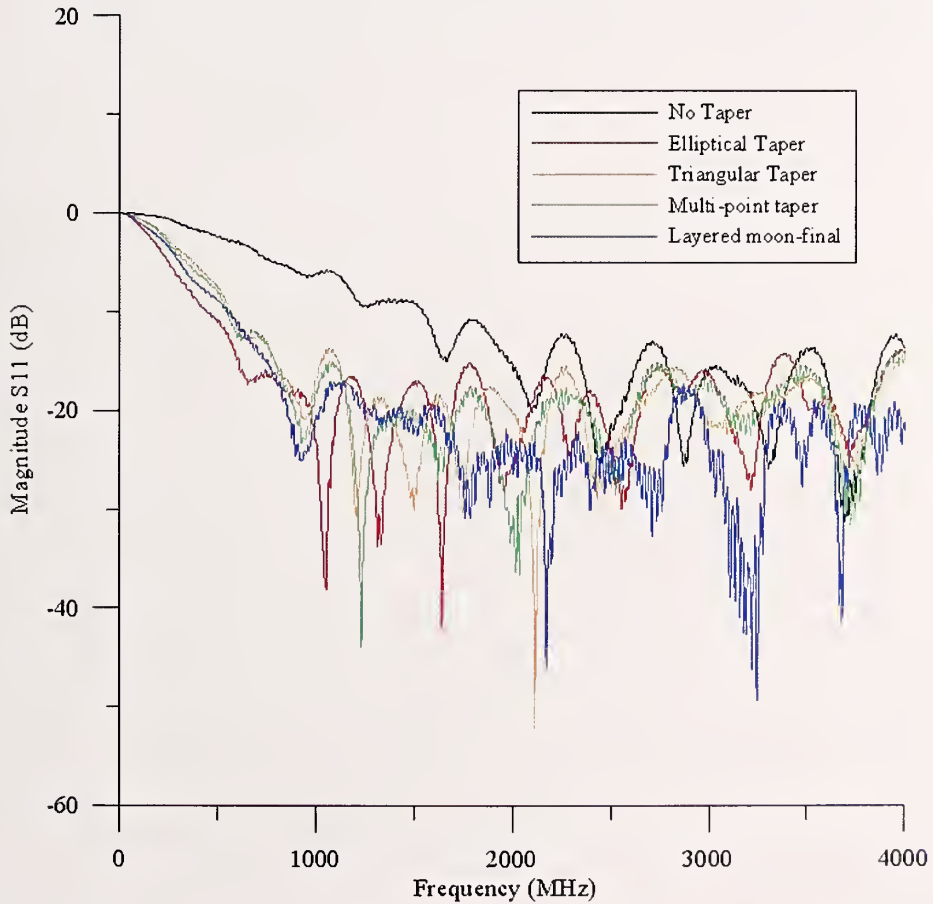


Figure 34. Reflection coefficient for various taper designs.

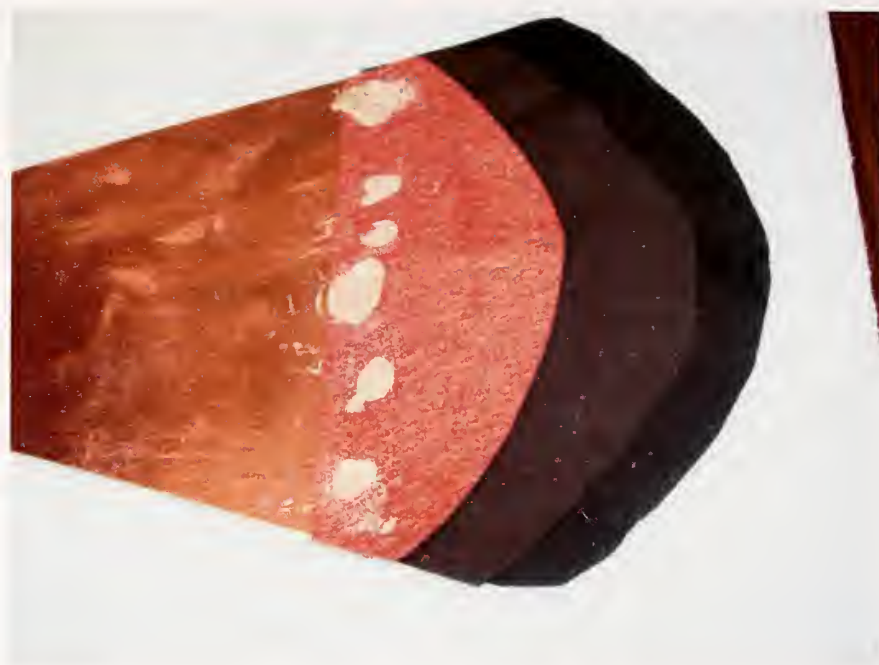


Figure 35. Close-up of the "layered-moon" resistive termination.

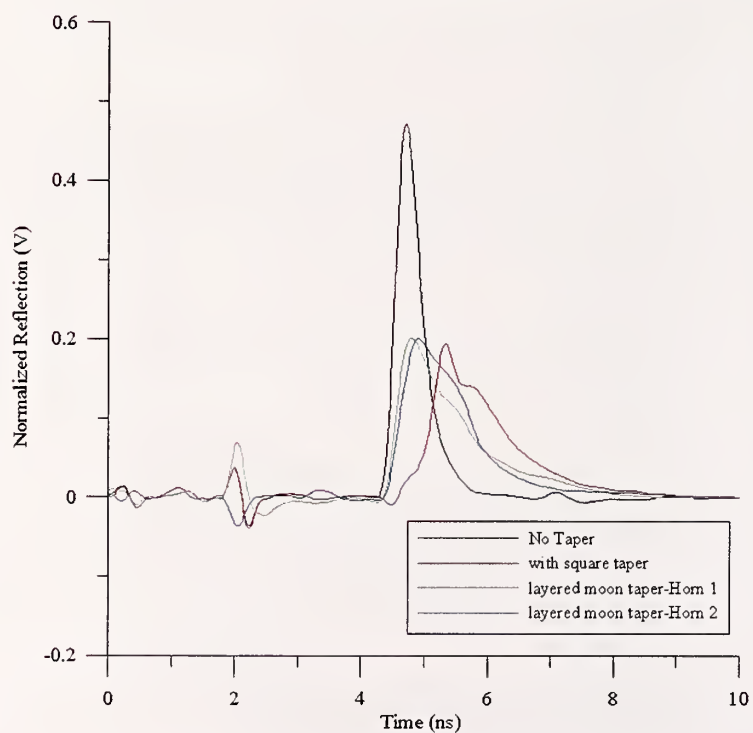


Figure 36. Input time-domain impulse response of resistively tapered TEM half-horn antenna.

## 2.5 Horn-to-Horn Responses and Measured Antenna Factors

Having discussed the design of TEM horn antennas, we now present some typical time-domain and frequency-domain signatures of these antennas to show both the short-impulse response and the constant-frequency horn-to-horn response indicative of TEM horn antennas. Figure 37 and 38 show the time-domain signatures of the 1.2 m TEM horn antenna and the 36 cm TEM horn antenna, respectively. Using the transmission measurements we can extract antenna factors and gain using the three-antenna method [29]. Figure 38 shows the measured antenna factor for three of our 1.2 m TEM horn antennas and two of our 36 cm TEM full-horn antennas, where antenna factor is defined in eq. (1). Due to a difference in baluns used, the red trace in Figure 38 is different from the other 1.2 m TEM horn traces.

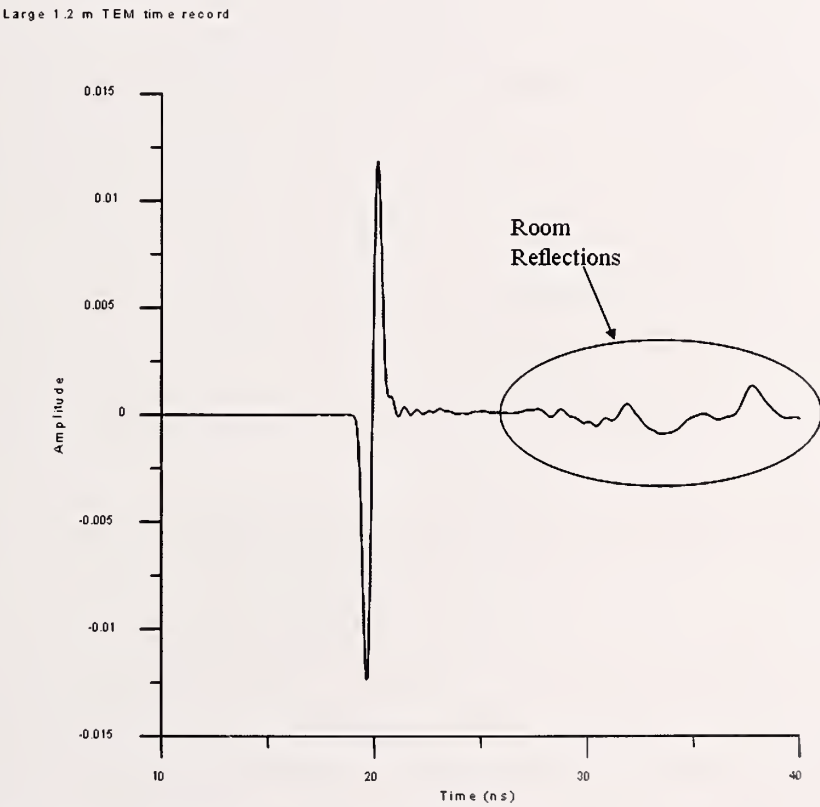


Figure 37. Horn-to-horn transmission measurement of our 1.2 m TEM horn antennas at a separation of approximately 3 m.

36.6 cm TEM antenna

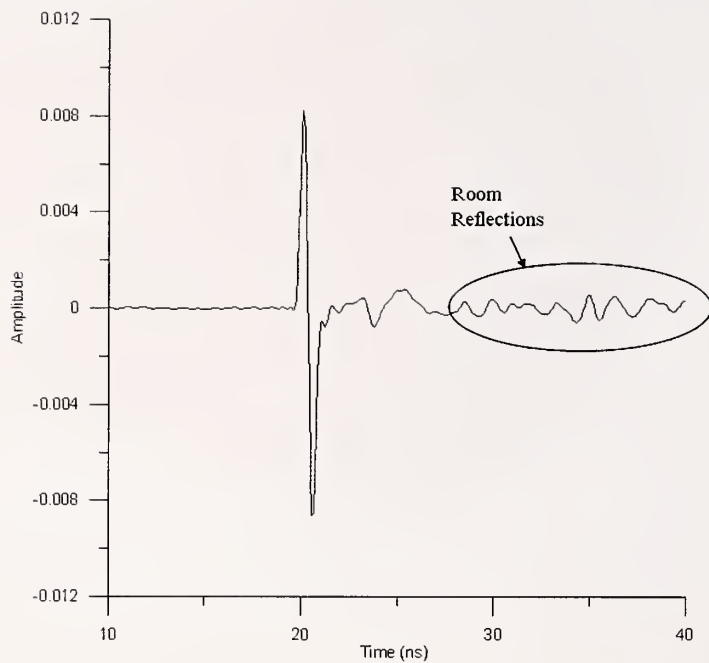


Figure 38. Horn-to-horn transmission measurement of our 36 cm TEM full-horn antenna at a separation of 3 m.

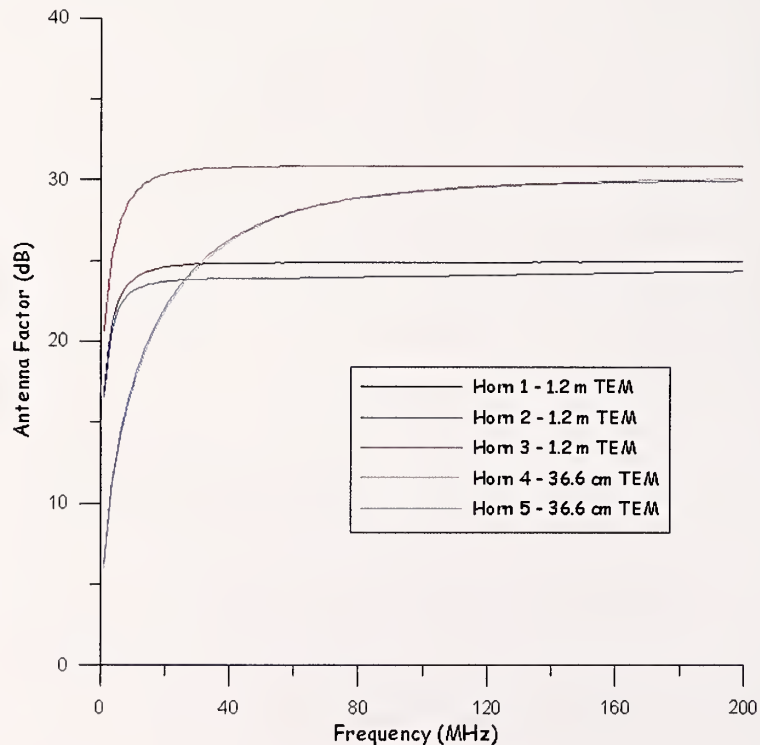


Figure 39. Measured antenna factor (AF) for three 1.2 m TEM horn antennas and two 36 cm TEM full-horn antennas.

### ***3.0 Antenna Numerical Design***

It is useful to model antennas by numerical methods as this allows us to look at design modifications, to understand antenna performance, and to diagnose design flaws prior to actual fabrication. We used a high-frequency numerical-modeling software package that employs the finite-element method. The selected software has a large database of materials and their electromagnetic properties and a number of boundary conditions that can be individually selected and incorporated into the model. The initial tetrahedral mesh can be automatically or manually dispersed throughout the volume. However, as the solution progresses, the mesh is automatically refined to increase accuracy. The solution is determined on a per frequency basis, but the solution can be extrapolated to other frequencies around the solution frequency. The post-processor allows one to look at fields, patterns, S-parameters, and impedances. Mathematical operators can also be applied to look at various other electromagnetic quantities of interest such as the Poynting vector.

We concentrated on different aspects of modeling for each of our TEM horn antennas. The 1.2 m TEM horn antennas were designed before numerical modeling was available. For this reason, we were interested in the performance of these antennas, namely the far-field radiation patterns, without having to do the extensive measurements required to obtain such patterns. We then compared these simulated patterns to specific cut-plane measurements taken in our laboratory. For the 36 cm TEM full-horn antennas, we looked at the impact of various design changes to understand their importance without having to construct modified antennas. We also looked at the far-field patterns of the current antenna design. Finally, the 36 cm TEM half-horn antenna was modeled to look at possible problems related to the truncated ground plane and to suggest design improvements.

#### ***3.1 Numerically Modeled and Measured 1.2 m TEM Horn Antenna Patterns***

This section discusses simulated and measured antenna patterns for a 1.2 m TEM horn antenna. A numerical model was compared to measurements taken in the laboratory. The numerical model allows us to understand the fields that radiate from the antenna and how they interact with the surrounding environment. Figure 40 shows the 1.2 m TEM antenna model used in the finite-element software package. The radiation boundary was a perfectly matched layer (PML) optimized from 100 MHz to 1000 MHz. A resistive taper was included in the model. Pattern measurements were taken in the time-domain laboratory on an 8 m x 8 m ground-plane

[30]. The experimental setup is shown in Figure 41. One horn was placed on a foam tower set on a turntable and rotated through  $360^\circ$  in  $3^\circ$  increments; the other horn was set on a foam tower and held stationary. The antennas were separated by a distance of 3.24 m. Both antennas were connected to a vector network analyzer (VNA) for measurements from 1000 MHz to 2000 MHz. The angular increments were chosen to allow near- to far-field transformations in this frequency range [30]. Our measurement facility contained two adjacent concrete walls and a ceiling at a height of 5 m. To minimize reflections from the walls and ceilings, time-gating, absorber, and measurement sweep time were utilized. In Figure 42, the applied time gate is shown by the rectangle between 13 ns and 30 ns. The horizontal ovals indicate room effects, and the vertical oval indicates a reflection from the horn feed. Figures 43 to 45 compare the measured and simulated antenna patterns for 100 MHz, 500 MHz, and 1000 MHz, respectively. It should be noted that the model used one antenna and an ideal monitor point, whereas the measurements were made using two antennas. This could account for the differences seen in Figures 43 to 45. Figure 43 shows the results for the vertical and horizontal polarizations at 100 MHz. Figure 44 shows the results for the vertical and horizontal polarizations at 500 MHz. The simulated results

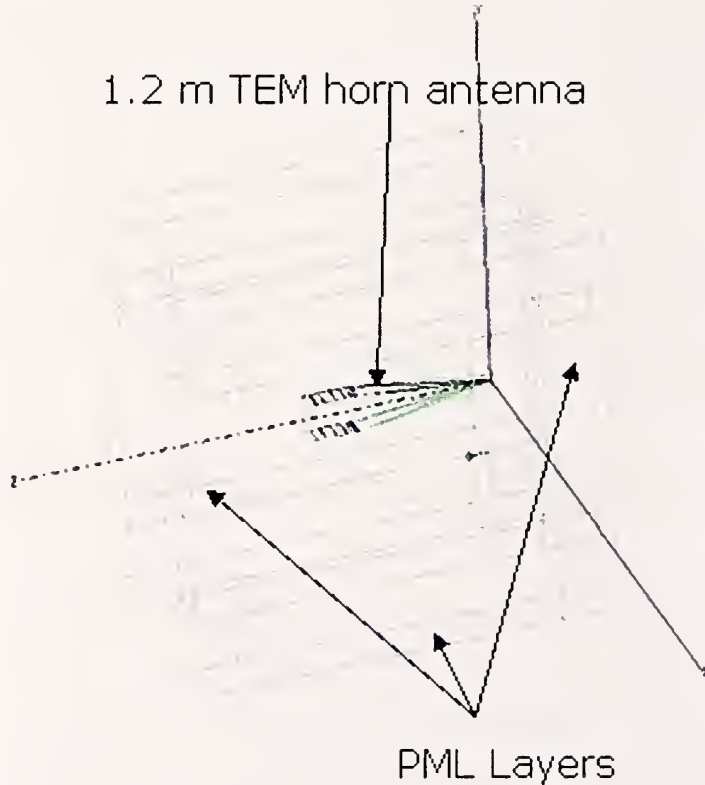


Figure 40. Drawing of 1.2 m TEM horn antenna in modeling program.

show good agreement to within a few decibels on boresight and to within 10 dB at various side lobes for the measured results. We also see more lobing at 500 MHz with simulated results quite comparable to measurements. Figure 45 shows the results for the vertical and horizontal polarizations at 1000 MHz. Although magnitudes tend not to be accurately modeled, the lobing patterns are represented reasonably well. These simulations allow us to look at the patterns and understand why we see phenomena such as larger ground bounce in the horizontal polarization at 500 MHz.

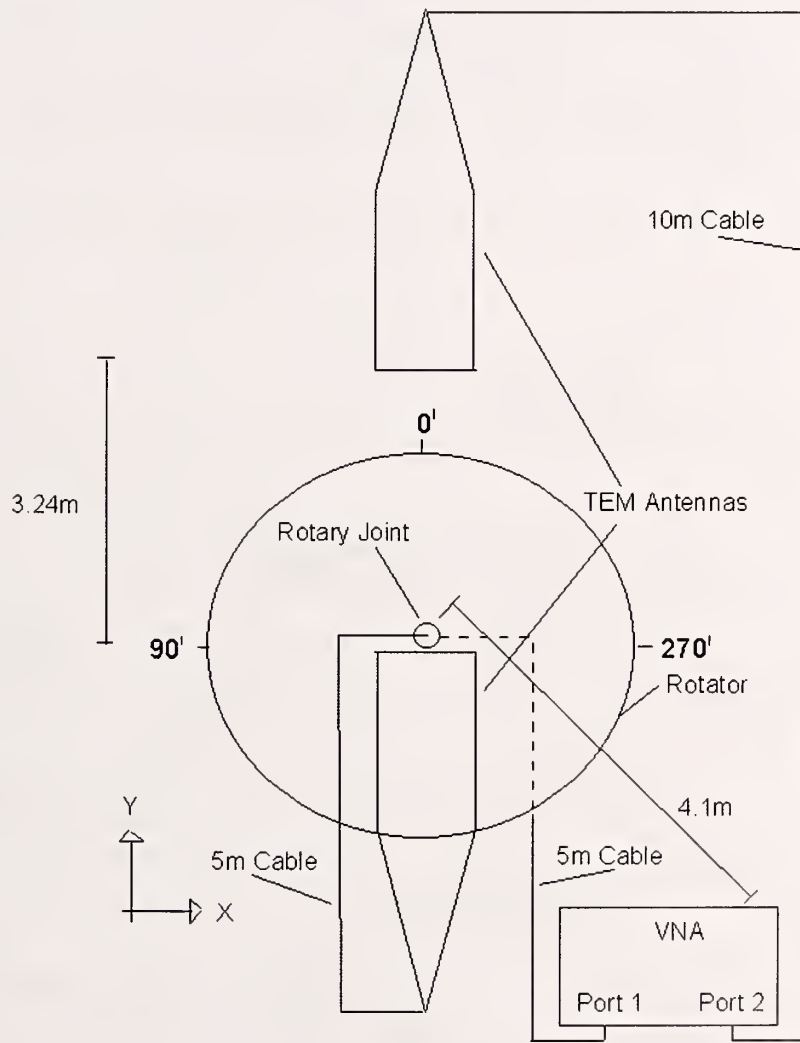


Figure 41. Experimental setup for 1.2 m TEM horn pattern measurements.

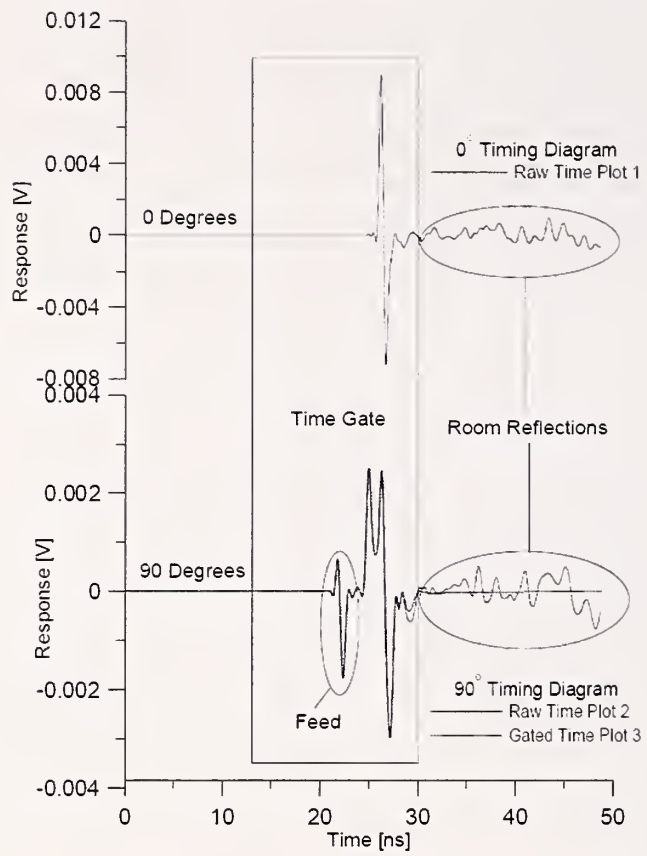


Figure 42. Time-domain graphs showing reflections from antennas and room.

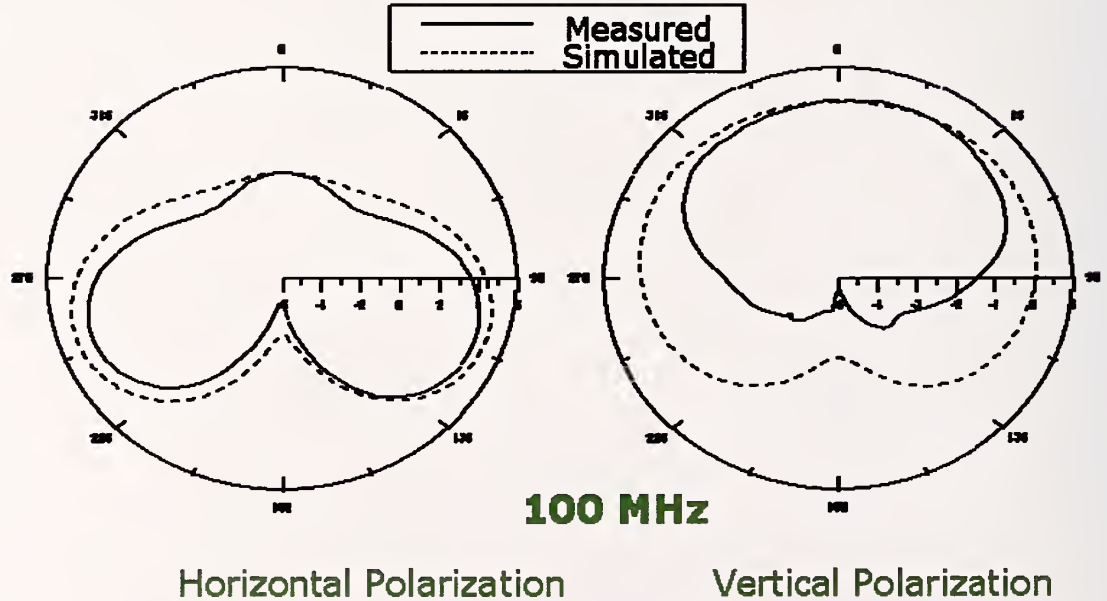


Figure 43. Pattern simulation and measurement at 100 MHz for 1.2 m TEM horn antenna.

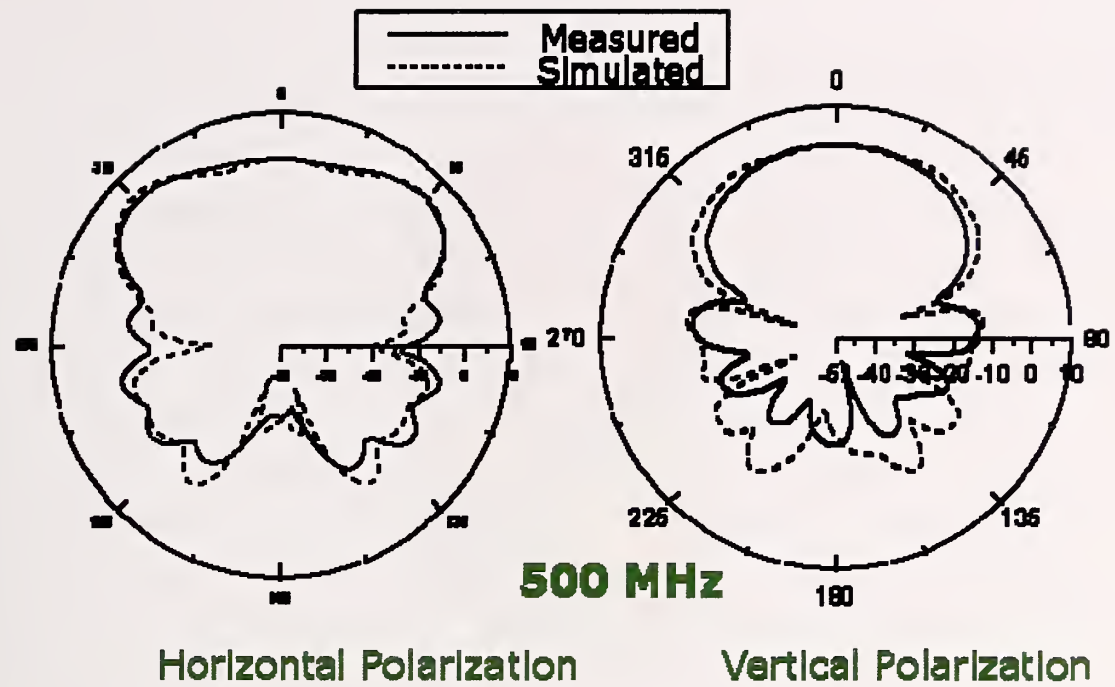


Figure 44. Pattern simulation and measurement at 500 MHz for 1.2 m TEM horn antenna.

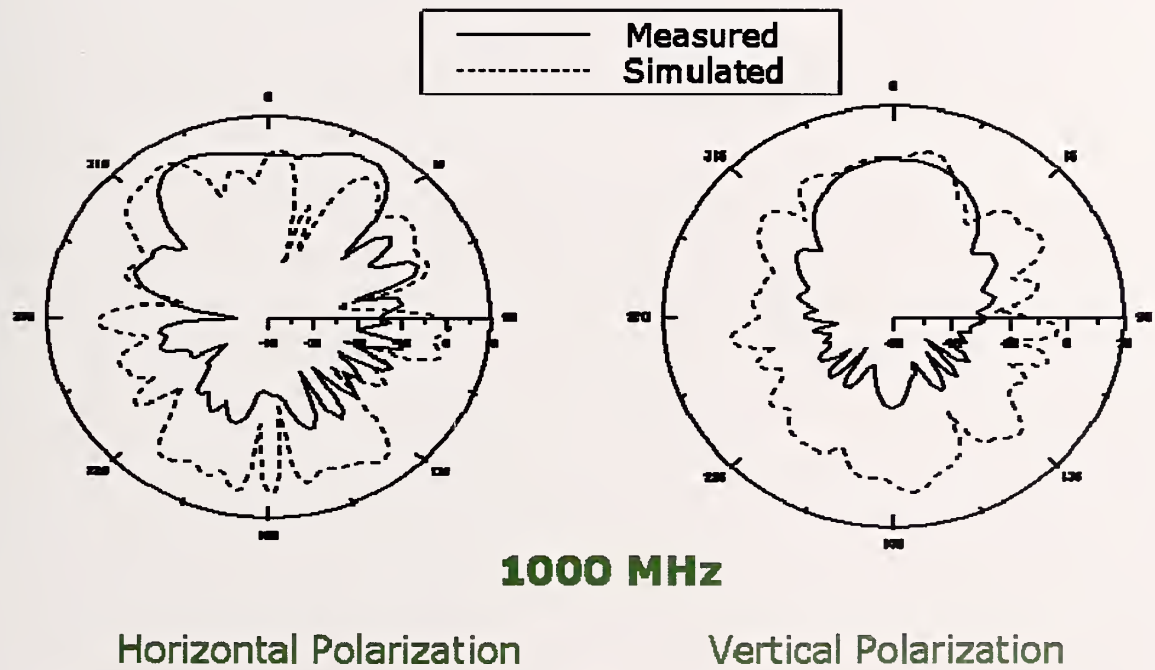


Figure 45. Pattern simulation and measurement at 1000 MHz for 1.2 m TEM horn antenna.

### 3.2 36 cm TEM Full-Horn Numerical Modeling

Our goal in modeling the 36 cm TEM full-horn antenna was to understand the antenna patterns and to look at pattern control using various design modifications. We looked at the antenna as originally assembled (which included the center ground plane), the effects of removing the ground plane, adding resistors to the sides of antennas to restrict fields, and curving the front edge of the apertures. Figure 46 shows antenna modifications made. The original 36 cm TEM design (including ground plane) is shown in Figure 20, Section 2.3.1. The center ground plane was grounded to the outer conductors of the incoming  $50 \Omega$  coaxial lines and then the two outer antenna elements were connected to the center conductors of the coaxial lines. We knew that the 1.2 m TEM horn antennas had a bifurcated pattern because of experiments and the numerical models shown in the previous section, and so we expected some pattern irregularities from the 36 cm TEM full-horn antennas as well. Figure 47 shows the antenna pattern modeled at 500 MHz, the difference between front lobe radiation and feed-point radiation (z-axis) is approximately 3 dB. The aperture of the antenna is pointing along the x-axis. Modeling showed us that more

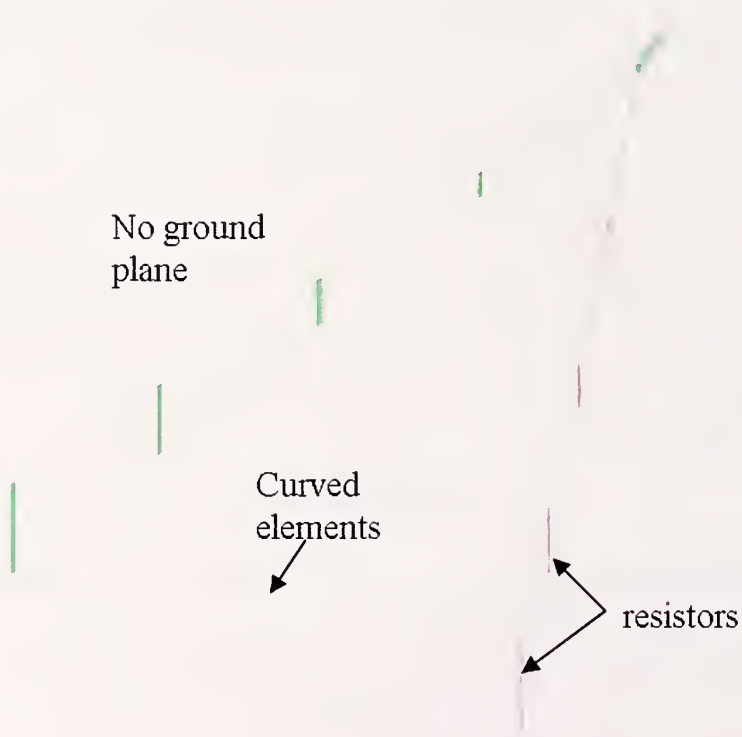


Figure 46. Simulated modifications for the 36 cm TEM horn antenna.

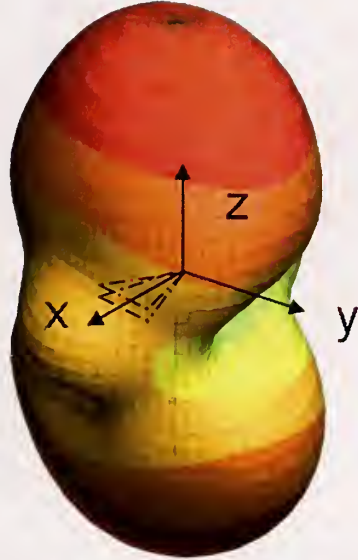


Figure 47. Modeled 3D far-field antenna pattern for 36 cm TEM full-horn antenna.

radiation was emanating from the feed-point than from the aperture of the antenna. The model shows that the difference is small. We confirmed this with measurements that are shown in Figure 48. The blue trace represents aperture radiation and the red trace represents feed-point radiation.

Figures 49 to 51 show far-field radiation patterns at three other frequencies with the antenna in the vertical polarization. At 875 MHz (Figure 49), the antenna is pointed toward the right edge of the page. Most of the radiation is coming from the aperture, but there are many side lobes. A bifurcated pattern is seen at 1500 MHz (Figure 50) and the antenna is now pointing toward the left edge of the page. The main fields are coming from the two antenna plates and the aperture center. A non-directive pattern is seen at 2800 MHz, as shown in Figure 51 and again the aperture is pointing toward the left edge of the page. We also looked at the total fields propagating both within and in the space immediately outside the antenna. This is shown in Figures 52 and 53 at a frequency of 500 MHz. The fields do propagate spherically out from the aperture of the antenna. In summary, the 36 cm TEM full-horn antenna with ground plane shows feed-point radiation, bifurcated lobes, and asymmetrical far-field patterns at higher frequencies.

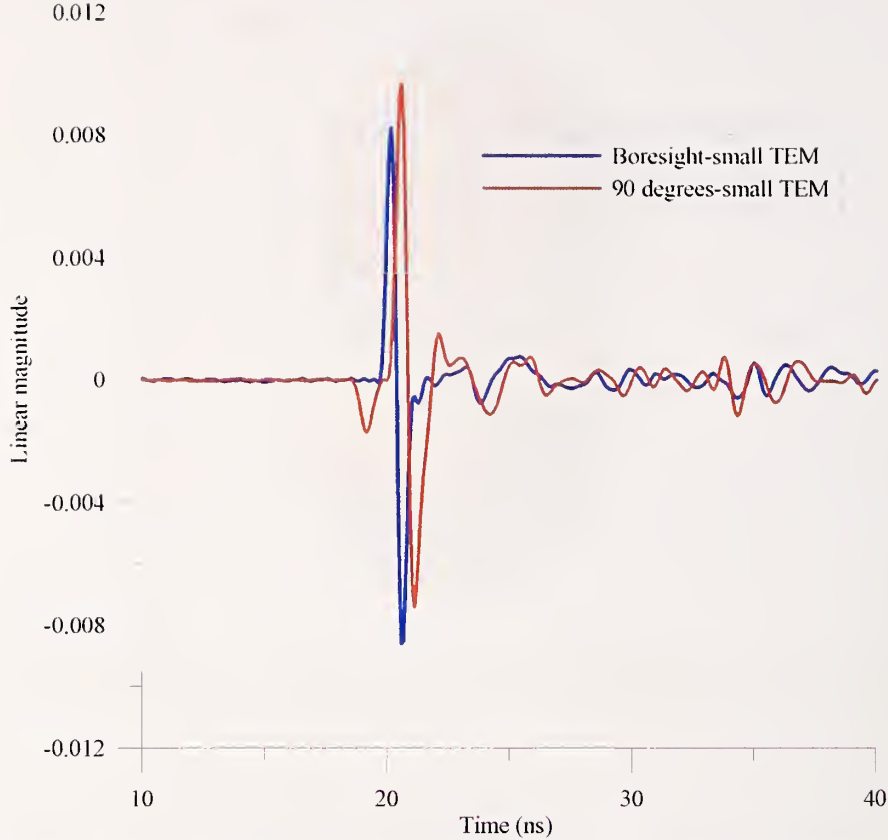
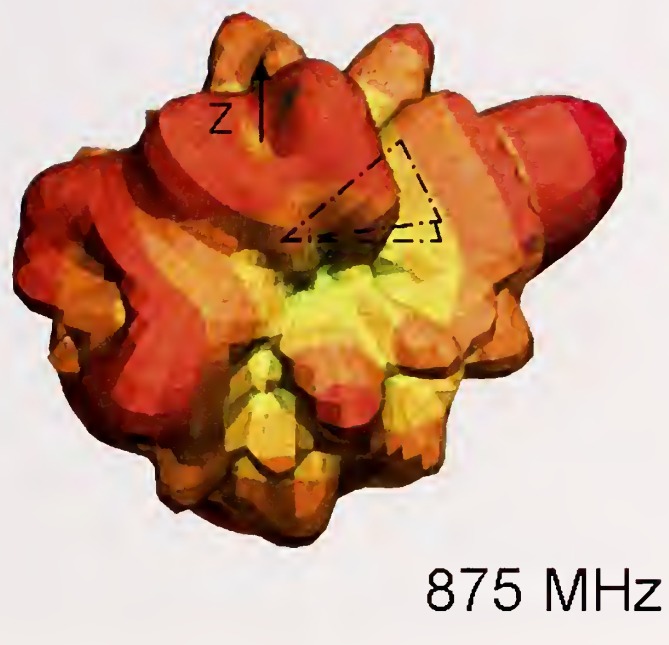


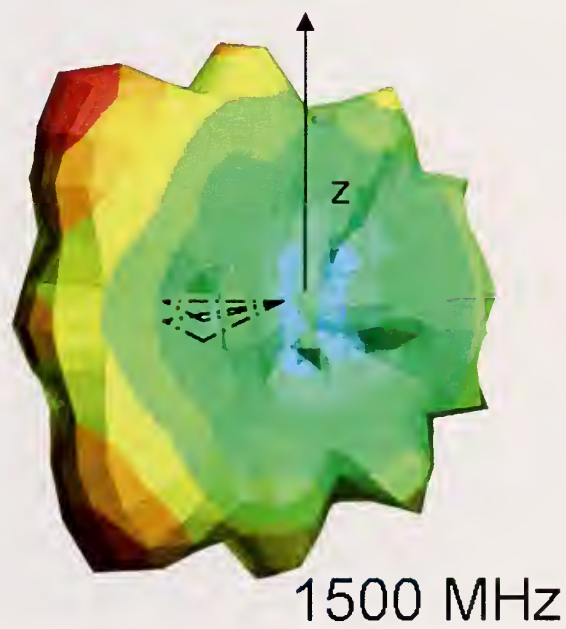
Figure 48. Measured time-domain waveforms along the boresight and feed-point radiation planes.

Modification of the original design included (1) removing the ground plane, (2) adding resistors between the two antenna elements to confine the fields, and (3) curving the front aperture plates to minimize reflection loss due to sharp edge transitions. The results of removing the ground plane are shown in Figures 54 and 55 at a frequency of 800 MHz. In Figure 54, we see that as the fields propagate from the aperture of the antenna they are distorted when the ground plane is included in the design. However, in Figure 55, the removal of the ground plane allows the fields to more easily transition into the free-field environment after leaving the aperture of the antenna. Figure 56 shows the fields in an antenna with the ground plane removed but without the resistors and curved apertures plates, and Figure 57 shows the antenna without the ground plane and with added enhancements. From these simulations we find the best improvement would be to remove the ground plane. We also attempted to suppress the feed-point radiation by placing a carbon sleeve over the feed-point of the antenna. Figure 58 shows that the sleeve did not decrease this radiation; experiments have verified this finding.



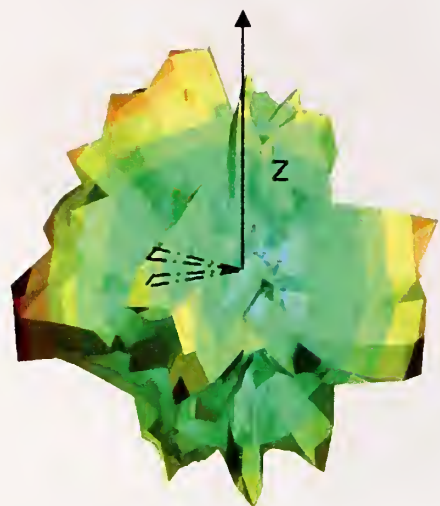
875 MHz

Figure 49. Simulated far-field antenna pattern at 875 MHz for 36 cm TEM full-horn antenna.



1500 MHz

Figure 50. Simulated far-field antenna pattern at 1500 MHz for 36 cm TEM full-horn antenna.



2800 MHz

Figure 51. Simulated far-field antenna pattern at 2800 MHz for 36 cm TEM full-horn antenna.

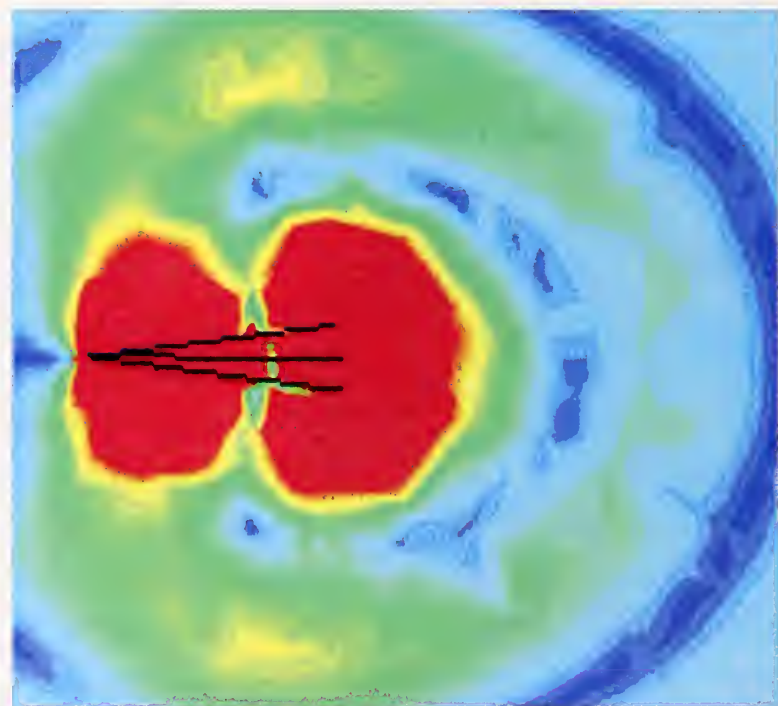


Figure 52. Total electric field in XZ-plane at 500 MHz for 36 cm TEM full-horn antenna with ground plane (side view).

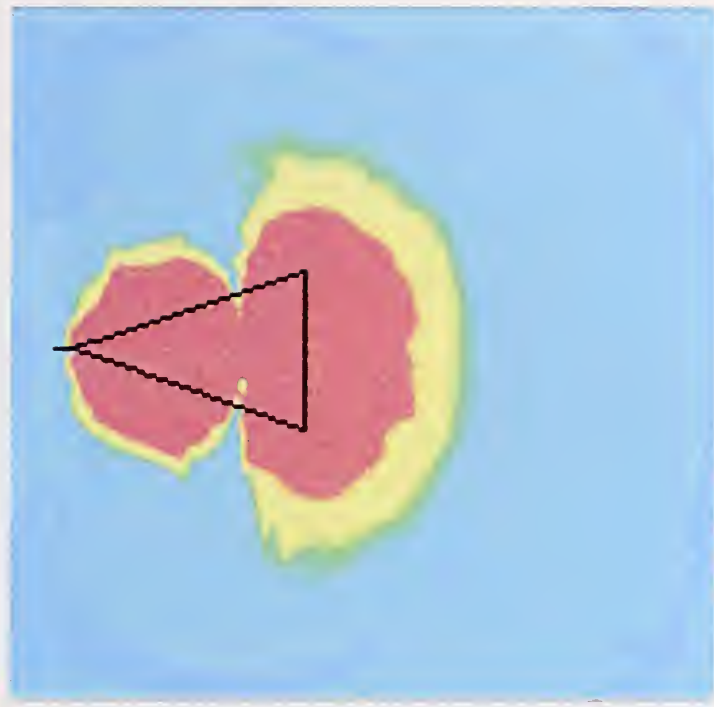


Figure 53. Total electric field in XY-plane at 500 MHz for 36 cm TEM full-horn antenna with ground plane (top view).



Figure 54. Total electric fields at 800 MHz for 36 cm TEM full-horn antenna with ground plane (top view).



Figure 55. Total electric fields at 800 MHz for 36 cm TEM full-horn antenna without ground plane (top view).

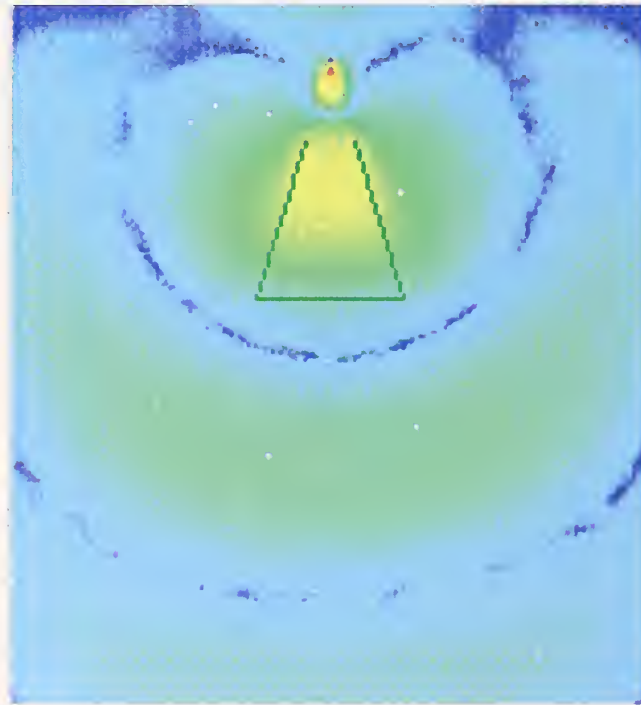


Figure 56. Total electric fields at 500 MHz for 36 cm TEM full-horn antenna without ground plane and no enhancements (top view).

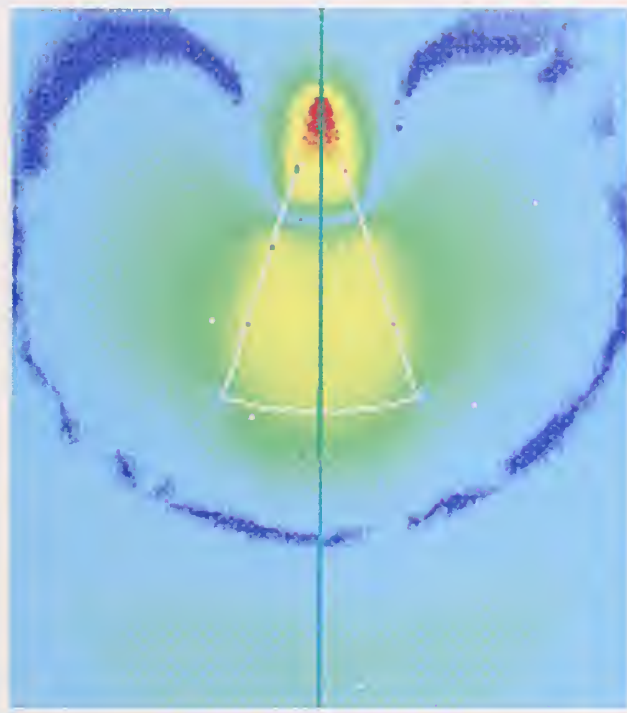


Figure 57. Total electric fields at 500 MHz for 36 cm TEM full-horn antenna without ground plane but will all enhancements (top view).

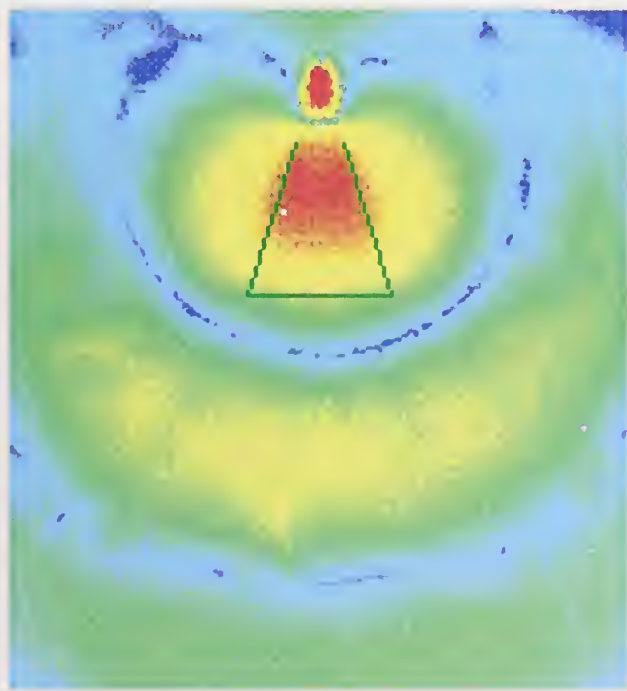


Figure 58. Total electric fields at 500MHz for 36 cm TEM horn antenna with carbon sleeve

### 3.3 TEM Half-Horn Numerical Design

The last numerical simulation was completed for a TEM half-horn antenna lent us by Professor R. Scholtz from the UltraRad Lab at the University of Southern California. We performed numerical simulations of the antenna for both the feed-point and pattern. This antenna is shown in Figures 59 and 60. The TEM half-horn sits on a ground plane that is 19.2 cm square. The antenna opening is 3.9 cm above the ground plane and is 18 cm in width at the aperture. This gives a width-to-height ratio of approximately 4.6. The tip of the antenna rests on the center conductor of the 3.5 mm coaxial cable that runs through the ground plane. The tip is soldered to the inner coaxial line. Both the ground plane and antenna plate are manufactured from copper with Styrofoam holding the position of the upper plate. This particular TEM half-horn antenna is designed to operate from 100 MHz to 4000 MHz. The modeled antenna is shown in Figure 61. For this particular antenna, we looked at the input return loss both for the original design and for a model containing a larger ground plane. We see that at the higher frequencies the model with the larger ground plane has slightly better return loss (Figure 62) compared to the original design (Figure 63). We looked at the original design and increased the ground plane by two times and recalculated the fields and antenna patterns for various frequencies.



Figure 59. Front view of USC TEM half-horn antenna.



Figure 60. Side view of USC TEM half-horn antenna.



Figure 61. Model for numerical simulations of a TEM half-horn antenna.

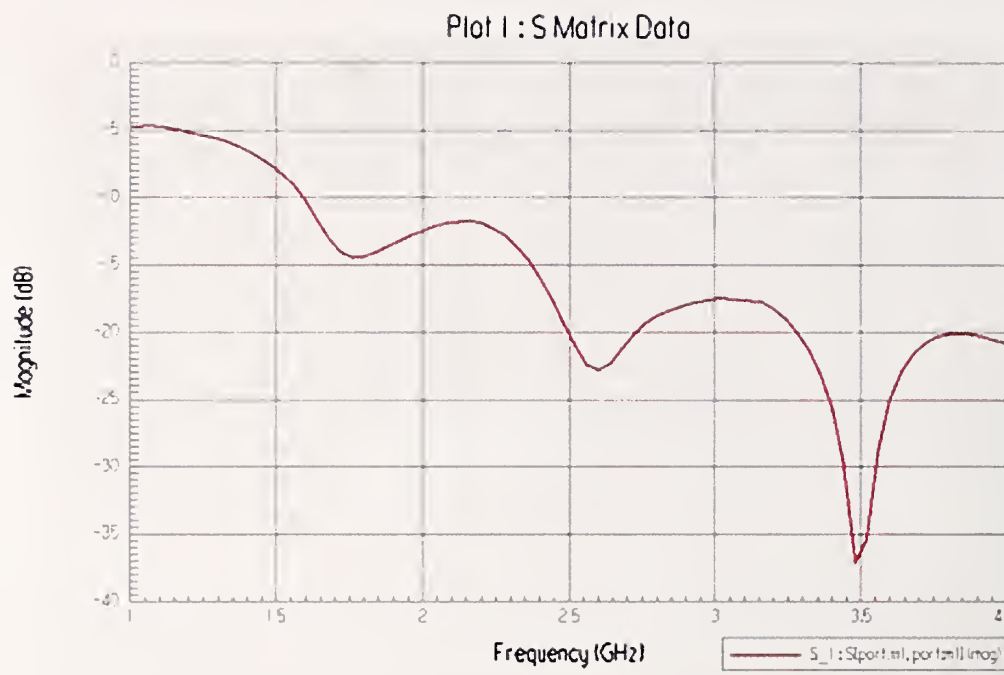


Figure 62. Input return loss for antenna design with larger ground plane.

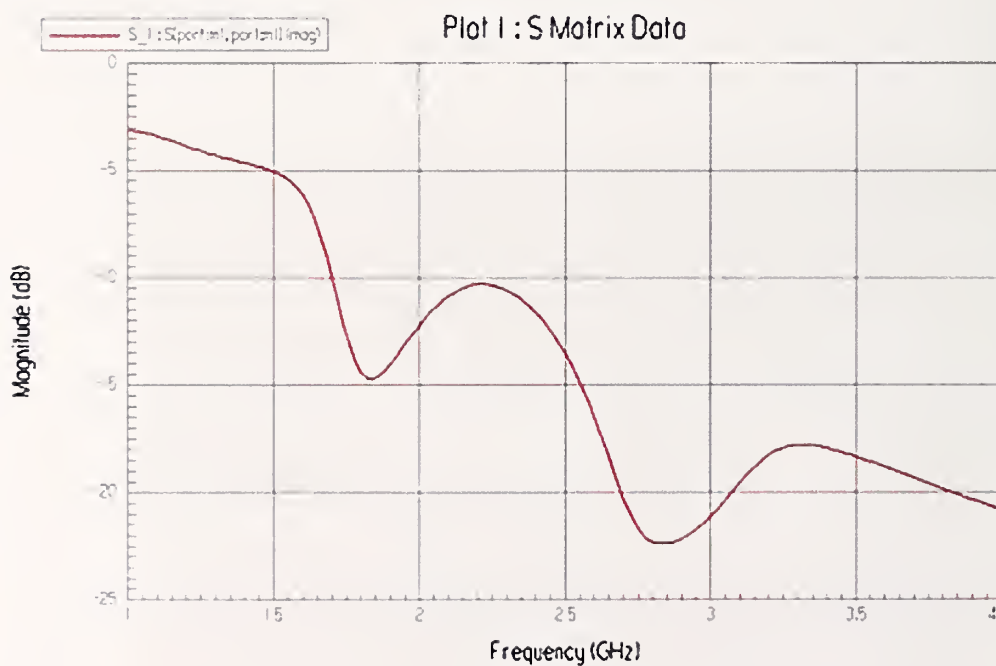


Figure 63. Input return loss for original antenna design.

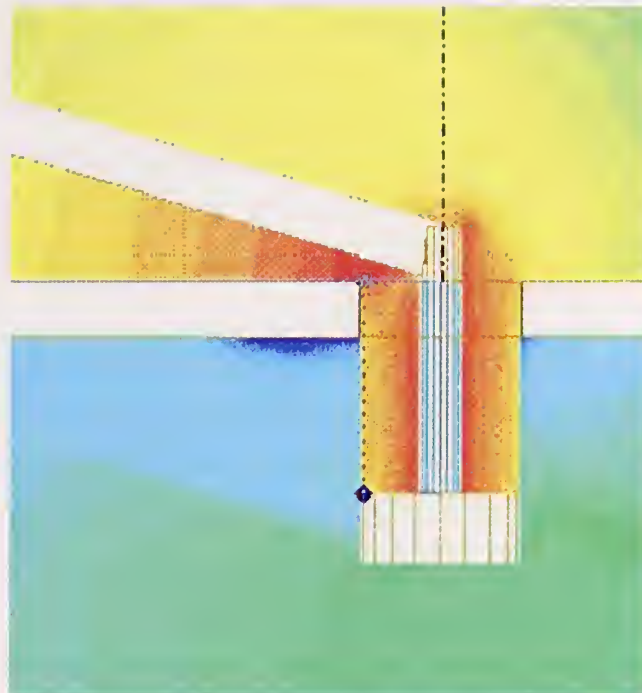


Figure 64. Close-up view of electric fields at modeled antenna feed-point.

Figure 64 shows a close-up view of the feed point between the incoming coaxial airline and the antenna plates. There is not much radiation emanating from this point, and the fields radiate out in a spherical pattern. Figure 65 shows a larger view of the original design, and illustrates the

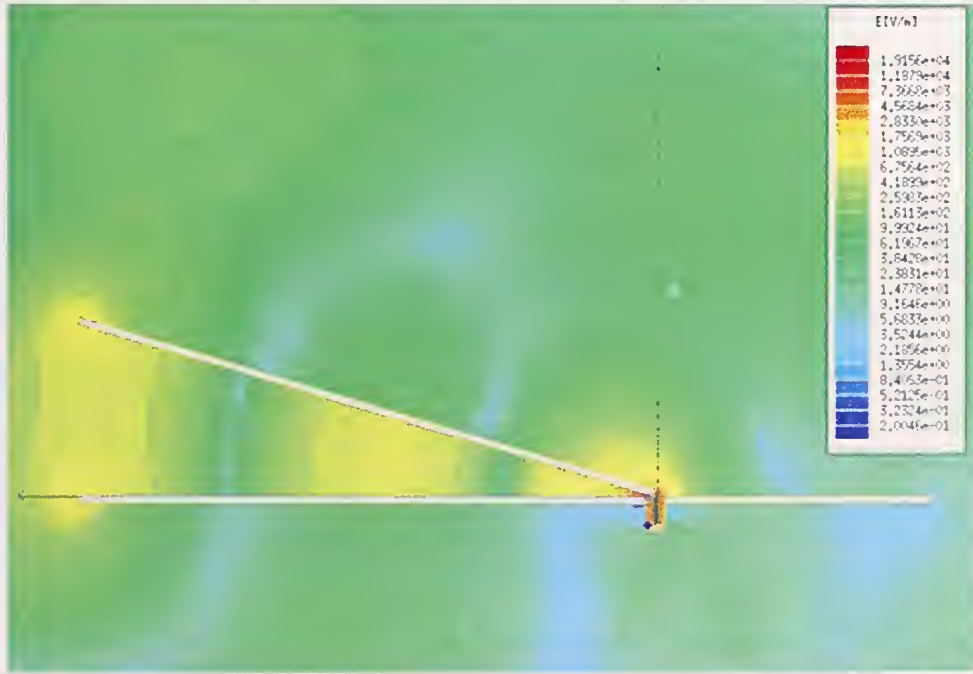


Figure 65. Total electric-field propagation along original USC antenna.

fields propagating along the antenna, the current discontinuity at the aperture of the antenna, and the feed-point radiation with respect to other field levels. We also see that the radiation diffracts around the ground plane, so that the whole structure radiates as the antenna instead of just from the aperture. As we enlarge the ground plane (Figure 66), more radiation propagates from the aperture than from the bottom of the ground plane so that we get more of a discone-like antenna pattern. Figures 67 through 74 show the far-field radiation pattern from these various antenna designs in the original design and then with the larger ground plane at various frequencies from 1000 MHz to 4000 MHz. In Figure 67, the antenna aperture is pointing out along the x-direction and the upper antenna plate is in the positive z-direction. With the smaller ground plane, the simulated far-field pattern confirms that there is radiation coming from the underside of the antenna, whereas the larger ground plane simulations of Figure 68 show less radiation on the underside of the antenna (z direction). The original design (Figure 69) still shows lobes emanating from the bottom of the ground plane. At 2000 MHz (Figure 70), we see that with a larger ground plane the radiation begins to give us the far-field antenna pattern characteristics of a discone antenna with the major lobe at approximately 45° in elevation. In figures 71 and 73, at 3000 MHz and 4000 MHz, we see radiation propagating along the bottom of the ground plane, but in Figures 72 and 74, with the larger ground plane, the pattern is more directional and emanates strongly from the aperture. In other words, the ground plane is acting like an infinite ground plane as the ground plane is enlarged; whereas, when the ground plane is truncated at the aperture of the antenna it acts like an antenna element causing radiation. In conclusion, a larger ground plane, as shown in Figure 26, is better for the 36 cm TEM half-horn antenna.

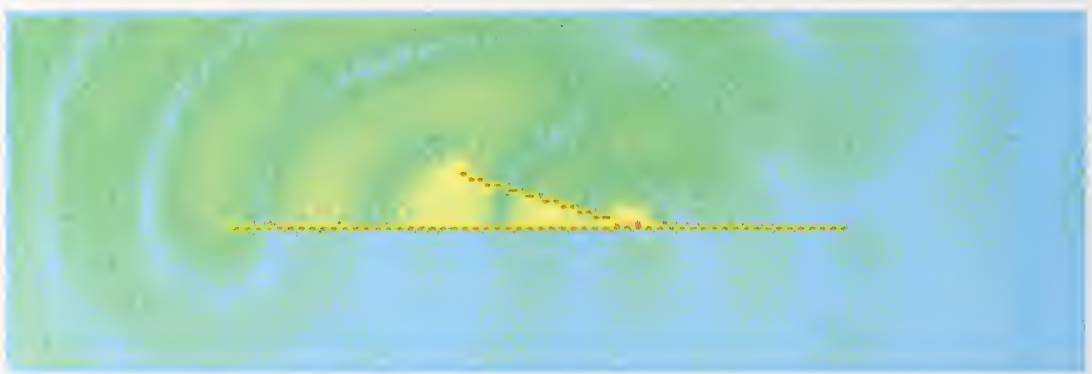


Figure 66. USC half-horn antenna modeled with a larger ground plane.

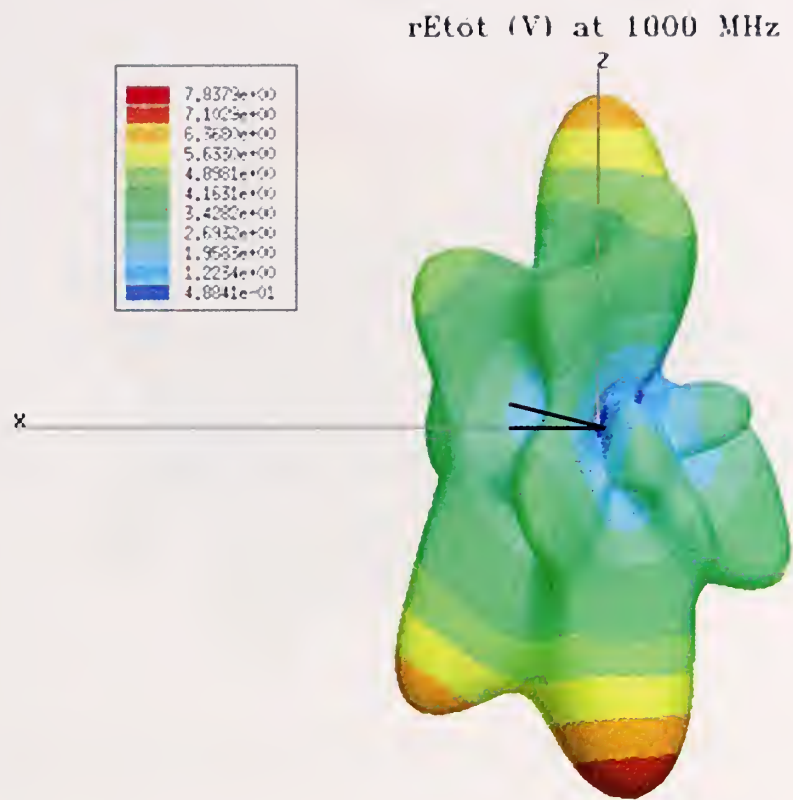


Figure 67. Side-view, far-field antenna pattern, original design.

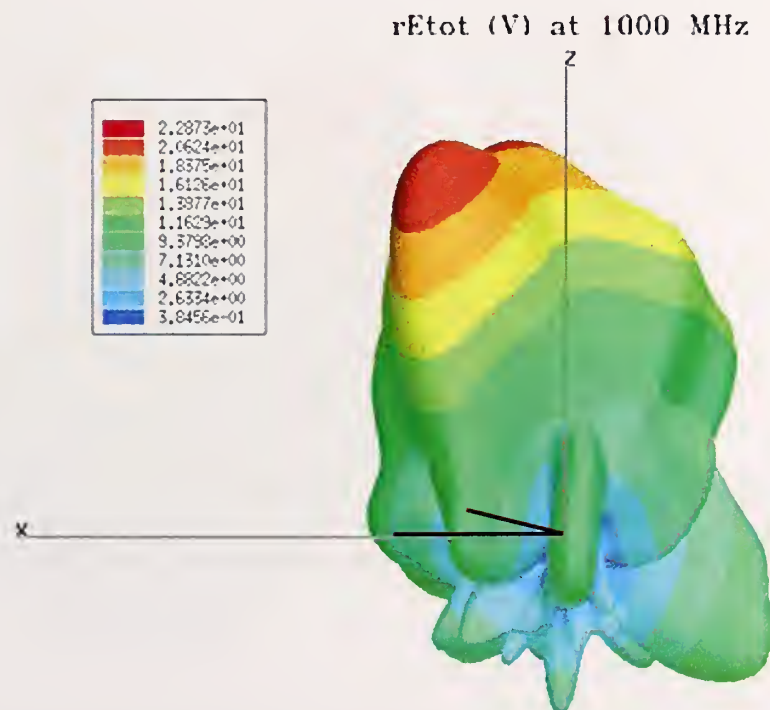


Figure 68. Side-view, far-field antenna pattern, larger ground plane.

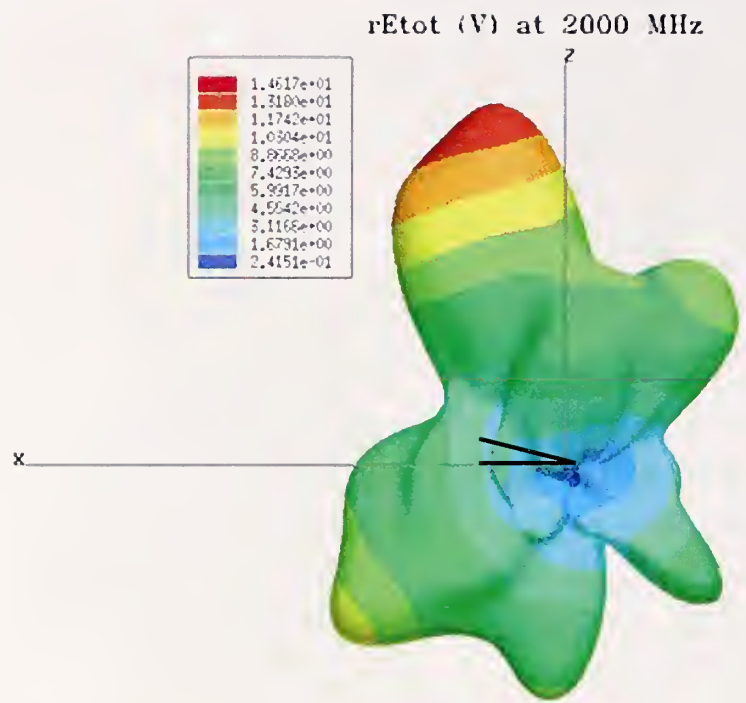


Figure 69. Side-view, far-field antenna pattern, original design.

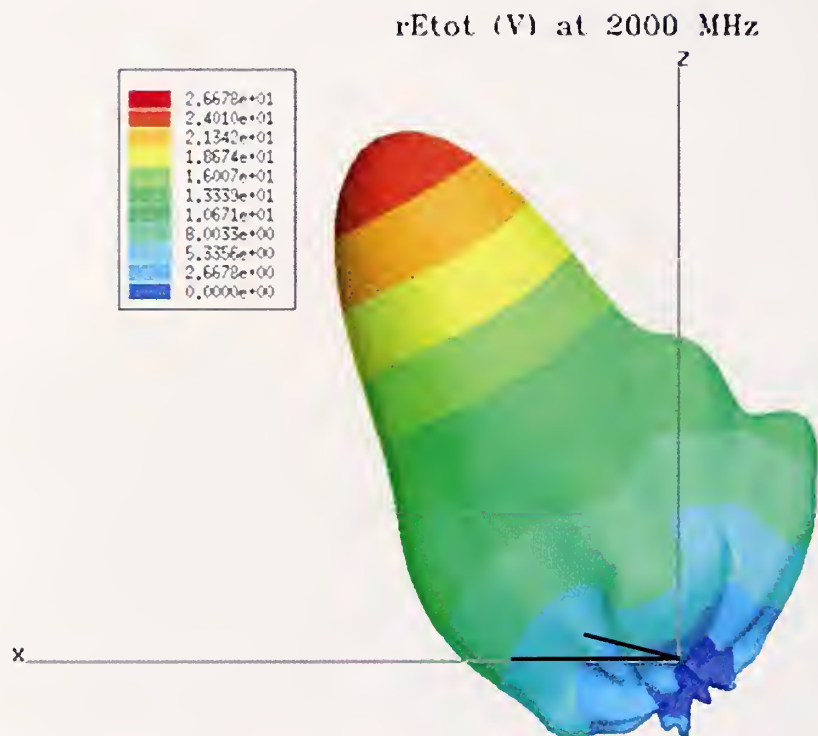


Figure 70. Side-view, far-field antenna pattern, larger ground plane.

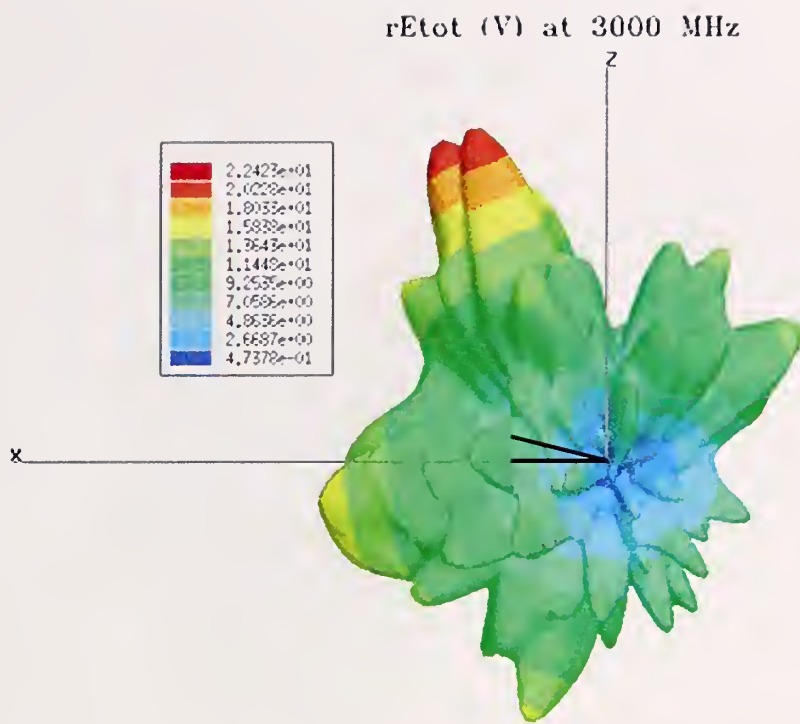


Figure 71. Side-view, far-field antenna pattern, original design.

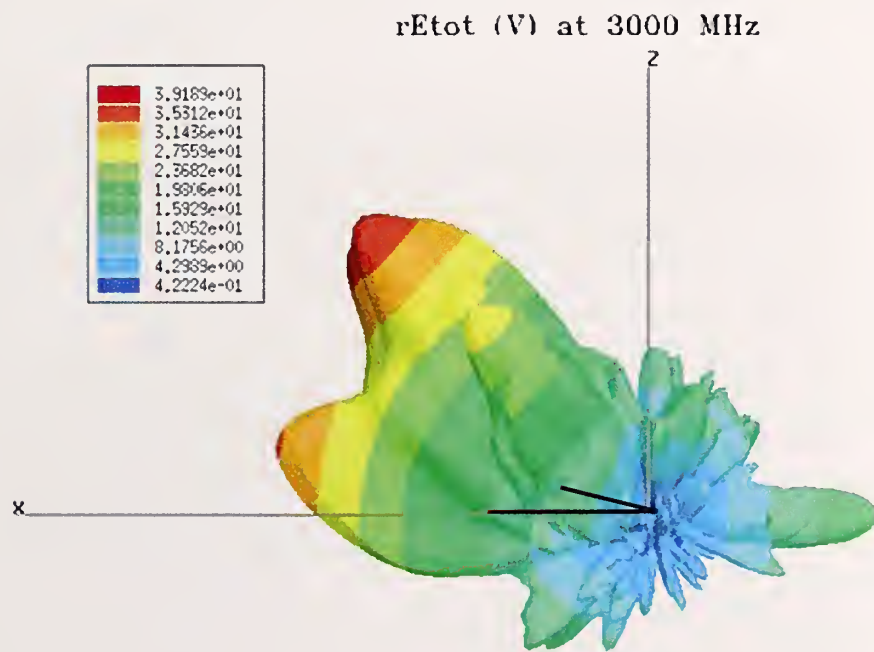


Figure 72. Side-view, far-field antenna pattern, larger ground plane.

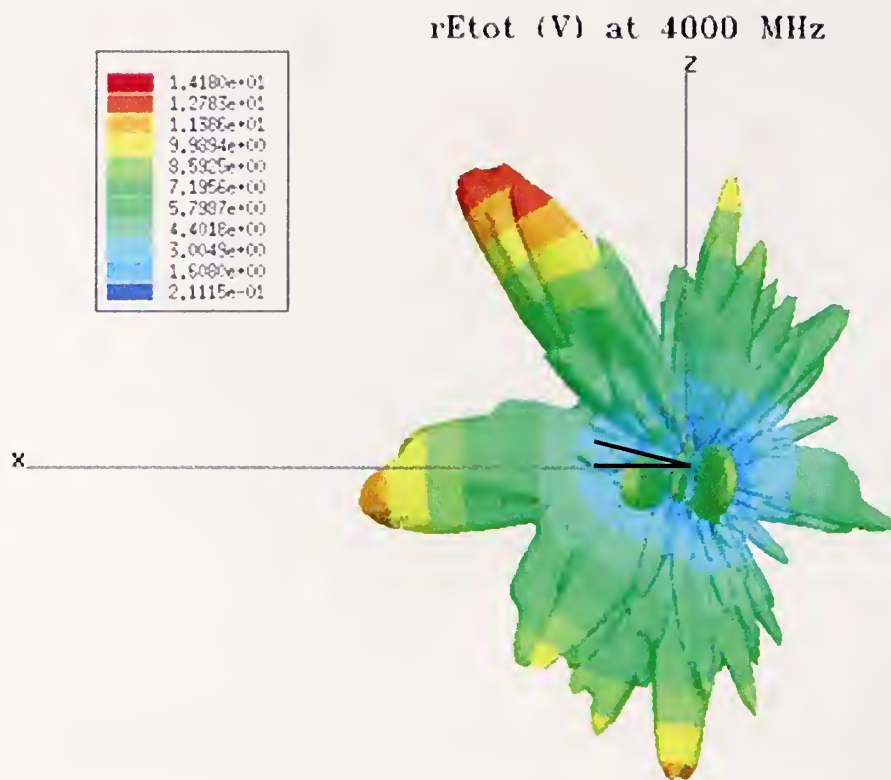


Figure 73. Side-view, far-field antenna pattern, original design.

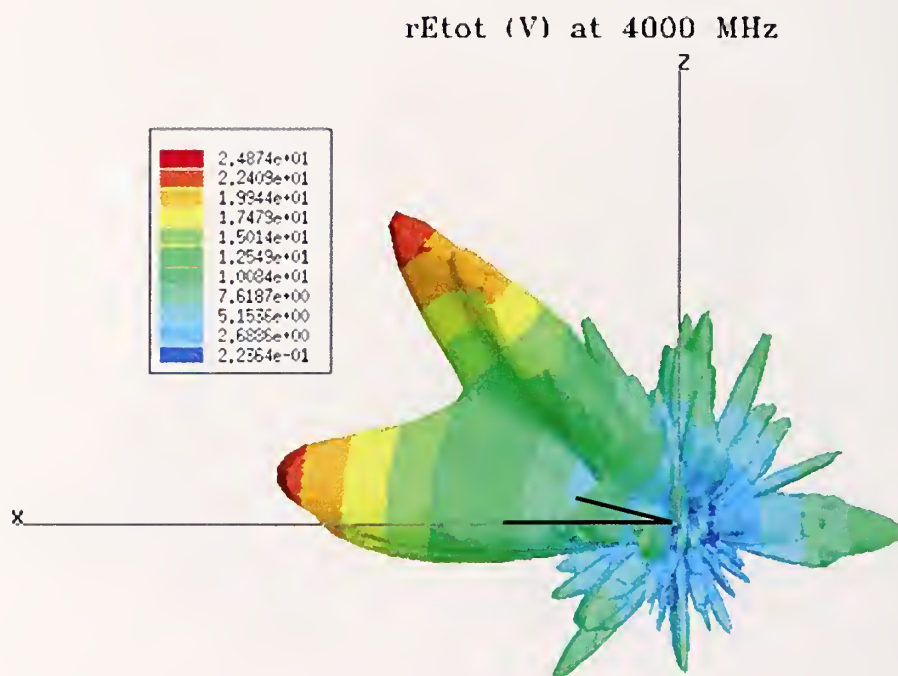


Figure 74. Side-view, far-field antenna pattern, larger ground plane.

## **4. TEM Horn Antenna Applications**

The following sections will discuss various measurement applications using TEM horn antennas. In each application, we find the TEM antennas useful because of their short-impulse response and linear phase. A brief description of the measurement effort is discussed and then an explanation is given of why the TEM horn antenna proved invaluable during each effort.

### ***4.1 Building-Material Measurements by Use of TEM Horn Antennas***

Our most recent application is to measure the dielectric properties of building materials. This project was supported by the Office of Law Enforcement Standards (OLES). The key benefit to using TEM horn antennas for building materials measurements involves their ability to be a part of a mobile unit. A free-field version of our TEM horn antenna measurement system can be transported to a specific location and used in-situ to measure the electromagnetic properties of materials. A picture of the ground-planed based setup is shown in Figure 75. This is a half-horn on a portable ground plane. It is a  $50\ \Omega$  system where the ground plane eliminates the need for a balun. This is a useful measurement system when the sample may be heavy to lift or when minimizing losses (especially balun losses) are an issue.



Figure 75. Experimental setup for measurement of reinforced concrete walls.

The measurement schematic is shown in Figure 76, and the measurement is performed as follows. The TEM half-horn antennas are separated by a specified distance, and the four S-parameters are obtained using a Vector Network Analyzer (VNA). This is known as a reference or background measurement. It includes reflections from the room and the antennas. In the second measurement, a  $1.5\text{ m} \times 1.5\text{ m}$  sample size of eighth-inch aluminum is placed symmetrically between the antennas and a metal-reference measurement is taken. The metal is then removed and a building material sample is inserted between the two antennas. All measurements have the background measurement in common and therefore spurious internal reflections can be removed by subtraction from both the reference measurement and the sample measurement in the time domain. What remains is the response due to the sample and the reference. Time-gating is applied here to remove any other responses that are not directly associated with the sample response. The sample response is then normalized by the reference response in order to obtain the reflection coefficient  $\Gamma_{\text{sample}}$  of the material sample as given in the

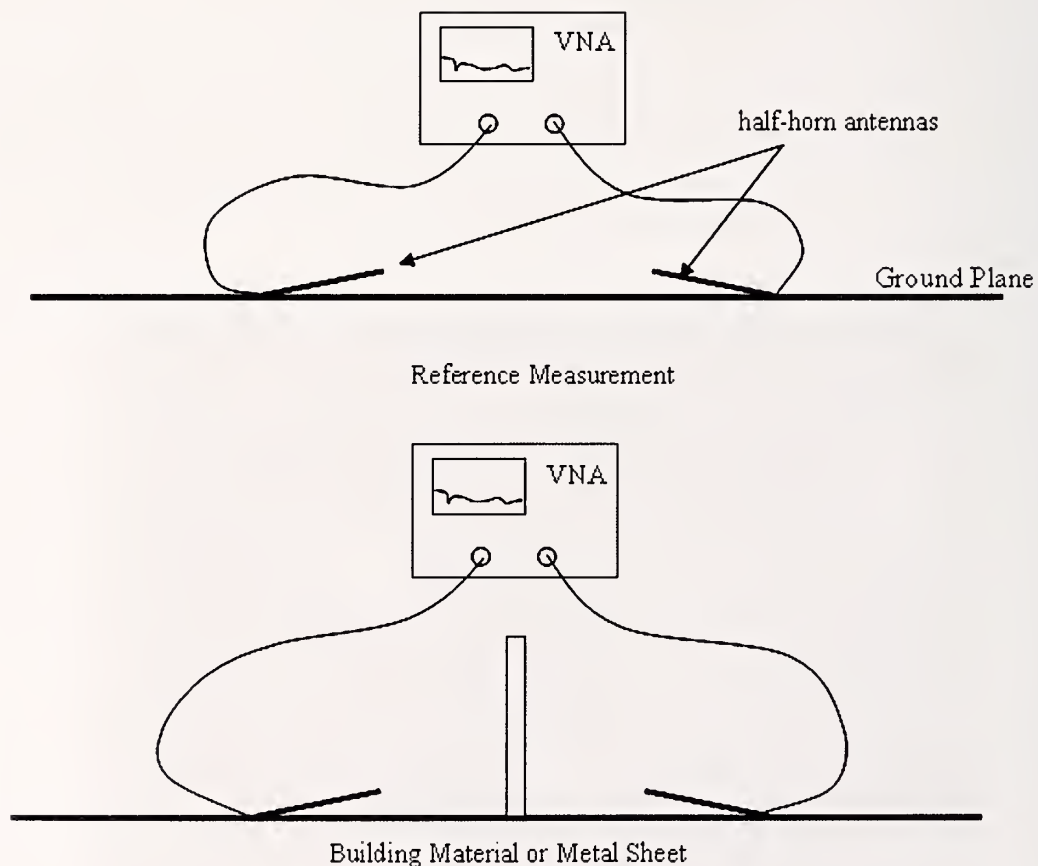


Figure 76. General measurement setup for reference and sample measurements.

following equation,

$$\Gamma_{\text{sample}} = \frac{S_{11\text{-sample}} - S_{11\text{-background}}}{S_{11\text{-metal-reference}} - S_{11\text{-background}}}. \quad (6)$$

Figures 77 through 80 show the data processing sequences for the reflection coefficient of the concrete sample. Figure 77 represents the original data from the network analyzer and includes the  $S_{11}$  concrete sample data (black trace) and the  $S_{11}$  background data (red trace). The initial reflections are from the coaxial transitions and feed-point of the antenna. The largest reflection is from the aperture of the antenna, and the last reflection in the black trace is from the concrete sample itself. The x-axis is time (nanoseconds) and the y-axis is the amplitude (volts) of the signal. After the background waveform is subtracted from the sample waveform and from the concrete waveform, we obtain the traces shown in Figure 78. We then want to extract only the information about the concrete sample itself so we time-gate the waveforms (Figure 79) in order to eliminate reflections not associated with the sample. After transformation to the frequency domain, we obtain the traces shown in Figure 80. The reflection coefficient of the concrete sample  $\Gamma_{\text{sample}}$  is shown as the blue trace. The transmission coefficient is obtained in much the same way. The equation governing this is given by

$$T_{\text{sample}} = \frac{S_{21\text{-concrete(gated)}}}{S_{21\text{-background(gated)}}}. \quad (7)$$

The waveforms for eq. (7) are shown in Figures 81 and 82. Figure 81 shows the measured time-domain transmission S-parameters for concrete (black trace) and background (red trace). We gate the background measurement as shown in Figure 79, and we gate the concrete waveform based on time-of-flight calculations. Figure 82 is the calculated frequency domain transmission coefficient for the  $S_{21\text{-concrete}}$  (black),  $S_{21\text{-background}}$  (red), and the normalized transmission coefficient of the concrete sample,  $T_{\text{sample}}$  (blue). From the four S-parameters, we can extract the permittivity of the concrete sample [31].

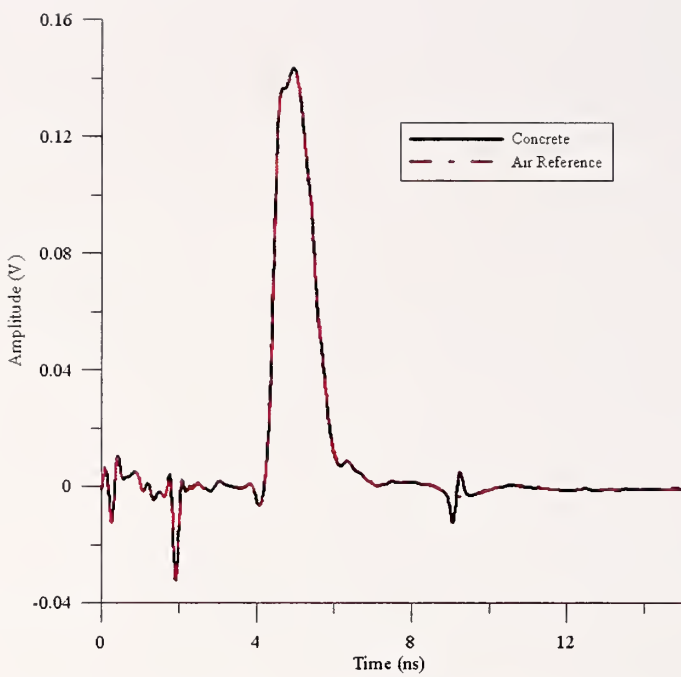


Figure 77. Input  $S_{11}$  measurement traces for air reference (red) and concrete sample (black).

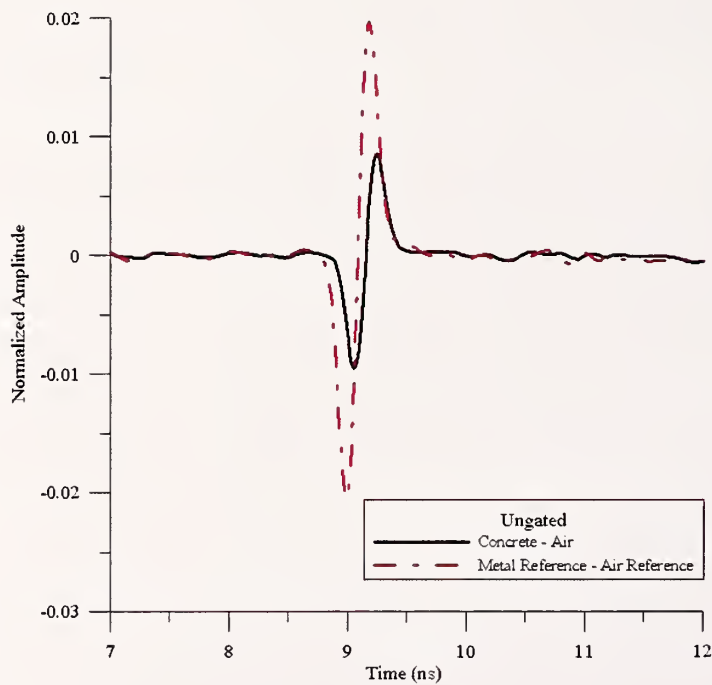


Figure 78. Subtracted  $S_{11}$  for concrete sample (black) and references (red).

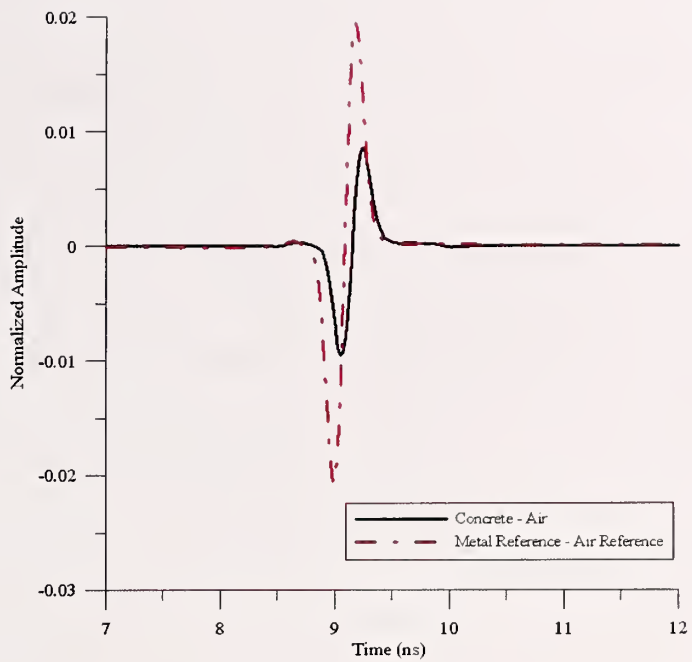


Figure 79. These are the gated waveforms for Figure 78.

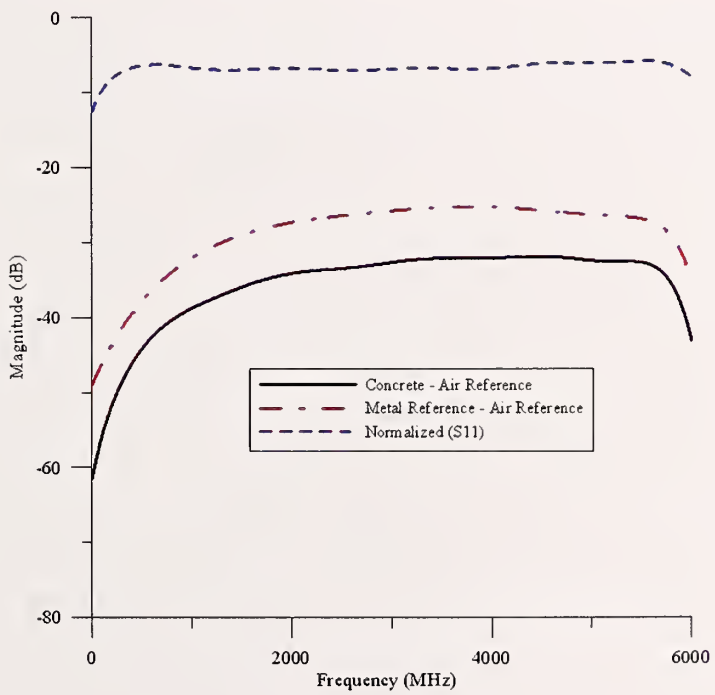


Figure 80.  $(S_{11\_concrete} - S_{11\_background})$  (black),  $(S_{11\_metal\_reference} - S_{11\_background})$  (red), and normalized or  $\Gamma_{sample}$  (blue) traces.

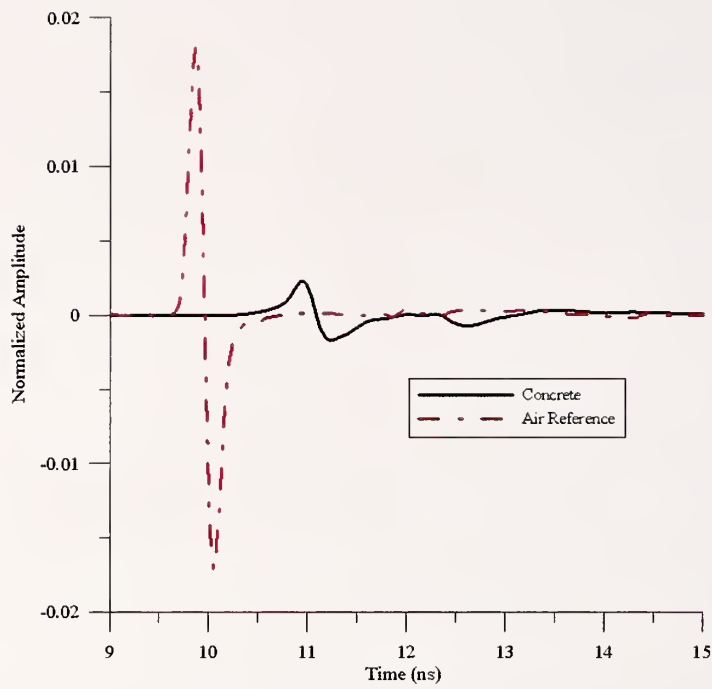


Figure 81. Time-domain traces for  $S_{21\_concrete}$  (black) and  $S_{21\_background}$  (red).

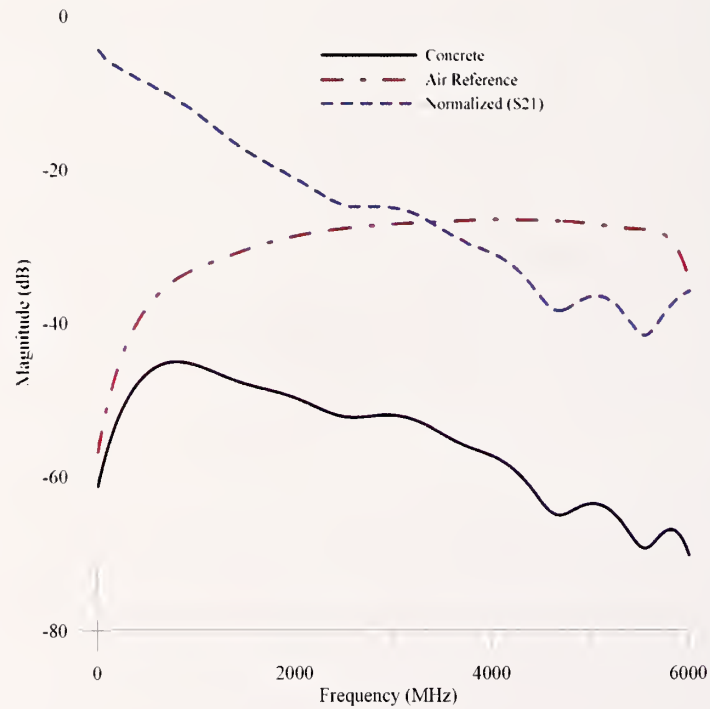


Figure 82. Frequency domain gated data for  $S_{21\_concrete}$  (black),  $S_{21\_background}$  (red), and the normalized transmission coefficient  $T_{sample}$  (blue).

## 4.2 Aircraft Measurements

One of the most common applications of our TEM horn antennas is the measurement of shielding effectiveness or penetration of various aircraft compartments. The equipment we use is a network analyzer, optical fiber link, cabling, and both the 36 cm TEM full-horn antennas and the 1.2 m TEM horn antennas. We take reference measurements in the same way as described above, but at a number of antenna separations, to look at  $1/r$  tendencies. Typically, the antennas are placed atop towers that align them with the aircraft windows. Two 1.2 m TEM horn antennas are placed on one tower in the vertical and horizontal polarizations and the 36 cm TEM antennas are placed on the other tower in the vertical and horizontal polarizations. After the references are taken, the 36 cm TEM full-horn antenna is placed inside an aircraft compartment and the other antenna with the 1.2 m TEM horn antennas is placed at various angular positions outside the aircraft at a specific distance; measurements are then taken (Figure 83). After data processing techniques are applied, we obtain the shielding effectiveness of various aircraft compartments.

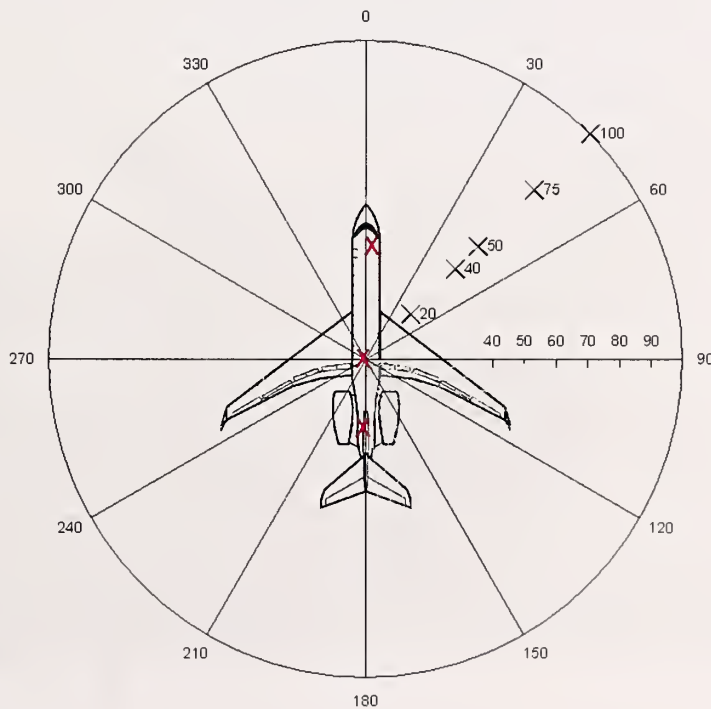


Figure 83. Diagram showing placement of antennas around aircraft for shielding-effectiveness measurements. Placement depends on space availability.

Figure 84 shows a photograph of a Federal Aviation Administration (FAA) Bombardier aircraft [32]. The FAA was interested in the shielding effectiveness of smaller aircraft such as this and asked NIST to collaborate. Three compartments were measured: (1) the flight deck, (2) the passenger cabin, and (3) the cargo compartment. The external TEM horn antenna was placed at approximately 30 m from the geometric center of the aircraft and rotated from  $0^\circ$  to  $190^\circ$ ,  $270^\circ$ , and  $330^\circ$  to  $355^\circ$  around the aircraft at increments of  $5^\circ$  and  $10^\circ$ . Results shown in the following figures are given for penetration into the passenger cabin with the external antenna at an angle of  $40^\circ$ . Figure 85 shows the time-domain decay of the fields within the aircraft. The initial direct antenna-to-antenna response is shown at around 75 ns. Figure 86 shows the 6 m free-space reference along with the actual penetration measurement into the aircraft. The free-space reference is deconvolved from the raw penetration measurement to obtain the normalized penetration of the aircraft shown in figure 87.



Figure 84. Bombardier aircraft used in shielding effectiveness measurements.

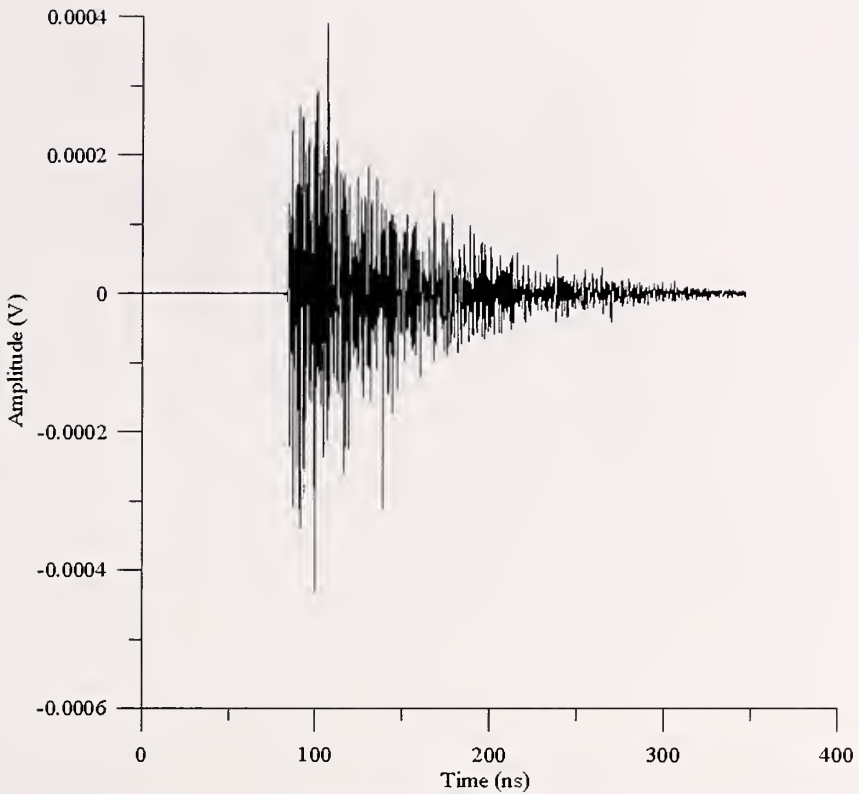


Figure 85. Time-domain waveform for penetration into FAA Bombardier aircraft.

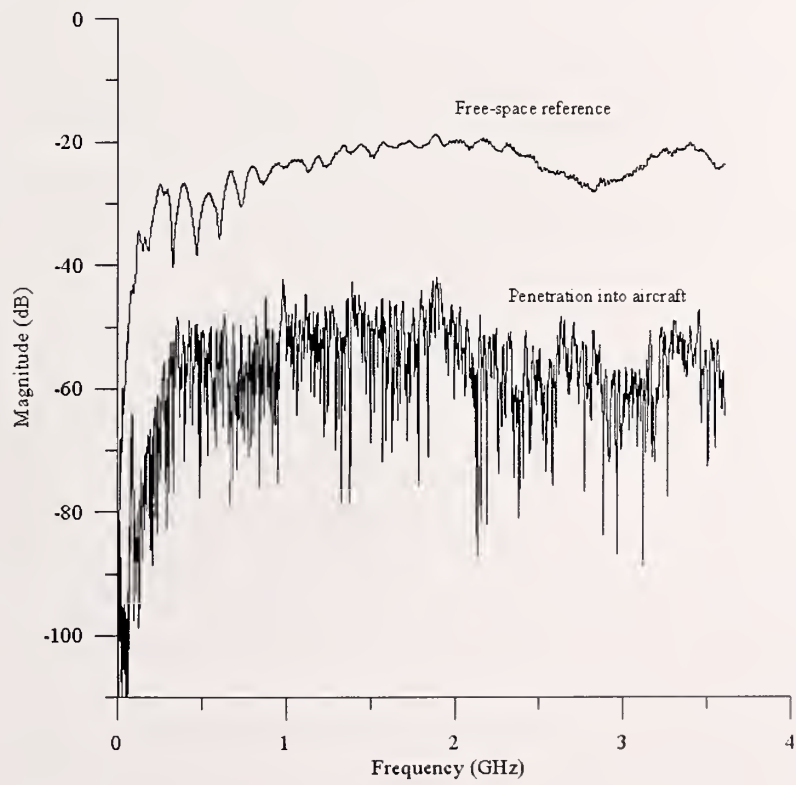


Figure 86. Free-space reference and penetration measurement into the aircraft.

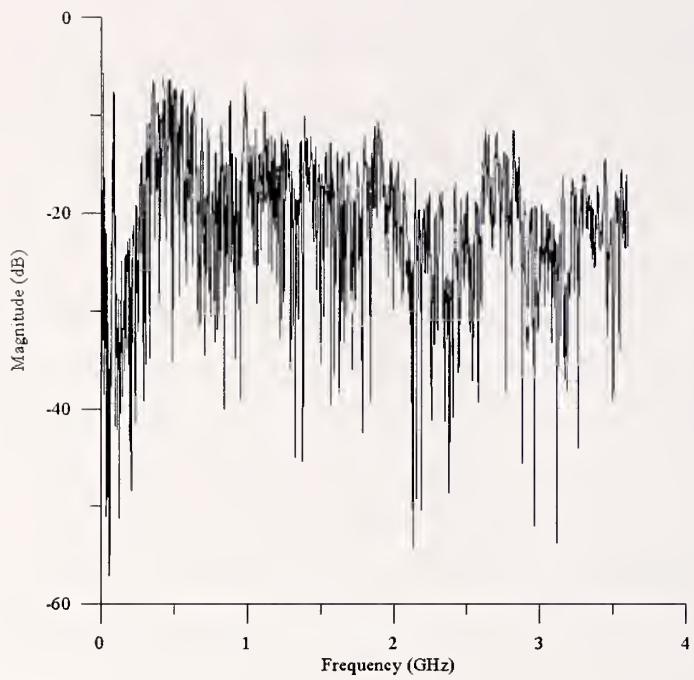


Figure 87. Normalized penetration for aircraft with external antenna at 40 degrees offset from center of aircraft at approximately 30 m. Internal antenna is in passenger cabin.

### 4.3 RF Absorber Measurements

These measurements tested a various samples of RF absorbing materials to determine their reflective properties across the frequency band from 30 MHz to 1200 MHz [33]. These samples were tested in our lab, which is a non-ideal environment, that is, a non-anechoic chamber. In this measurement, reflections are recorded at both normal incidence and oblique incidence, and after digital signal processing, the properties of the absorber are obtained.

Open area test sites (OATS) may be difficult to use because of the high ambient signal levels, inclement weather, and limited availability. Therefore, EMI and EMC measurements are more commonly conducted in anechoic chambers, which require the use of RF absorbing materials across a specific band of frequencies. Thus, the optimization of the chamber is a must, which leads to a need for the accurate characterization of the absorber. The tests conducted at NIST allowed us to characterize the properties of the absorber by using small quantities of material. The equipment used in these tests involved the 1.2 m TEM horn antennas and the VNA to collect data in the frequency domain. Fourier transforms were used to move the data into the time domain, and gating was applied to isolate scattering events related exclusively to the absorber. The resulting data were inverse Fourier-transformed to show the frequency response of the absorbing material.

The testing method is similar to that given in Section 6.1 for concrete measurements, wherein the reference is taken without the sample and then the sample is inserted in order to obtain the reflection coefficient as given in eq. (6). Figure 88 shows how an oblique-incident measurement is taken. The antennas are placed at equal angles from the normal and are pointed at the absorber.

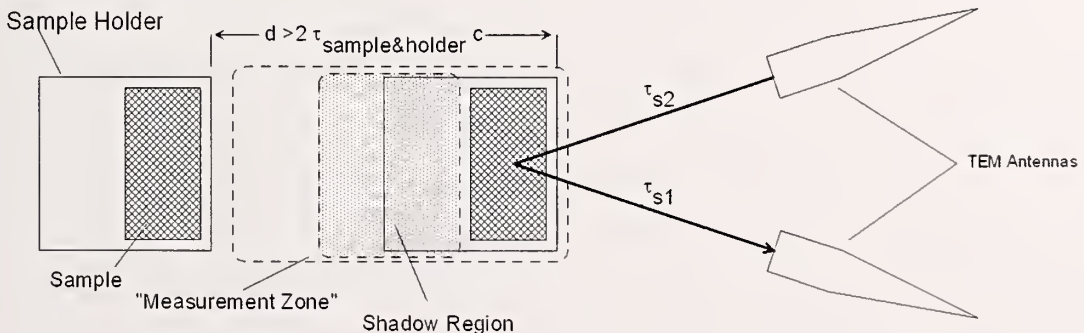


Figure 88. Movement of the sample in and out of the measurement zone  
For background subtraction.

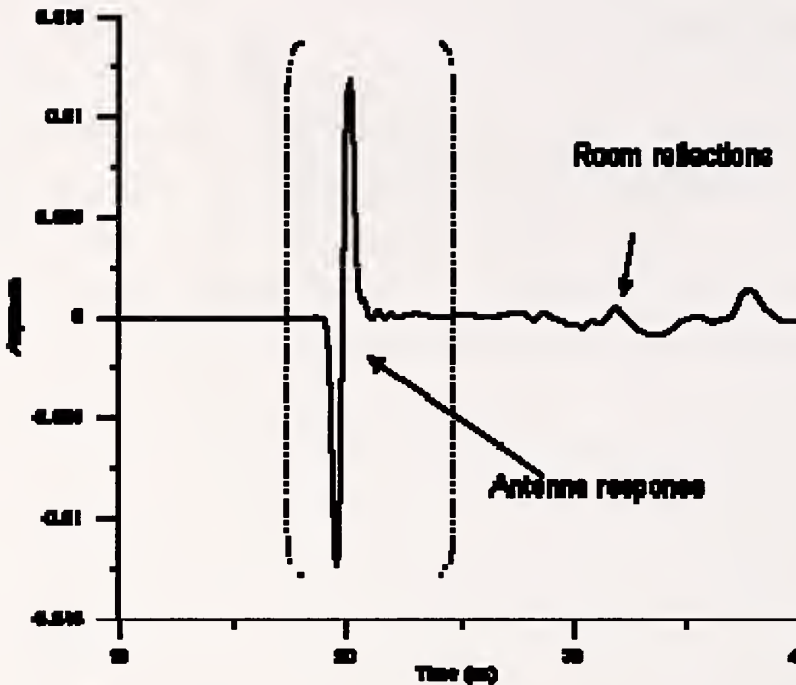


Figure 89. Impulse response of 1.2 m TEM-horn antenna shown by the dashed parentheses.

This background subtraction eliminates systematic effects from the measurements, or, in other words, common reflections from the measurement environment. Both normal and oblique measurements were made was in order to determine the curvature effects and to look at the various timing incidents. Oblique-incidence absorption is important in chamber design. Figure 89 shows the 1.2 m TEM horn antenna response in the time domain. The impulse response is approximately 2 ns for the 10 % points and precedes any room reflection or ground bounce. The two plots in Figure 90 show a normal incidence measurement of the absorber in our laboratory environment. The time domain allows us to look at events that happen in time. The TEM horn antennas allow us to resolve individual events because of their short impulse response. The impulse response of a log-periodic antenna was shown in Figure 2 and is roughly 40 ns in duration. If we were to use log-periodic antennas to measure the absorber, we would be unable to gate the waveform because the impulse response would make the edge effects and room reflections unresolvable. The detailed paper [33] discusses the effects of using various gates and how to optimize this gate. The same graph as shown in Figure 90 is also presented for oblique-incidence measurements in the original paper.

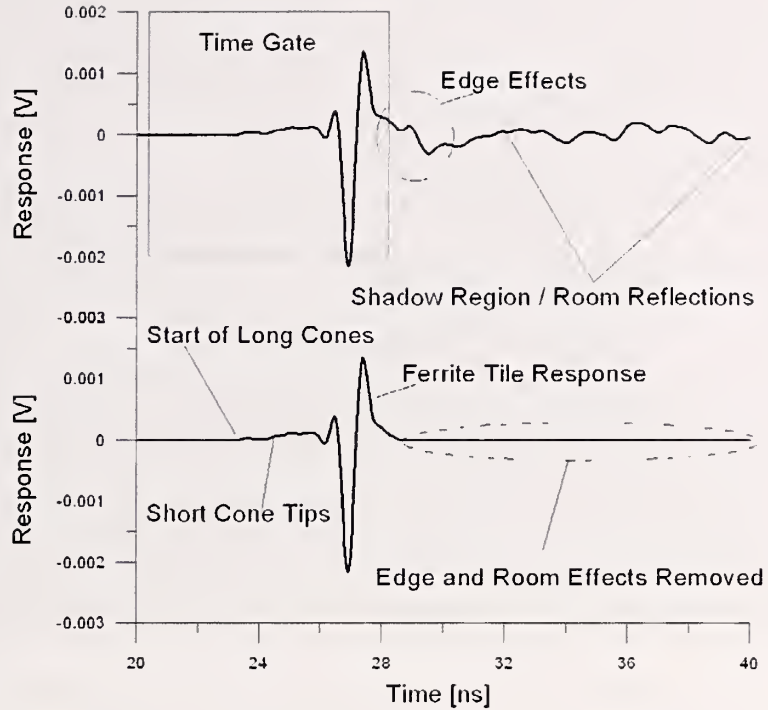


Figure 90. Time-domain gating of absorber measurements.

#### 4.4 Shelter Evaluations

Another evaluation was taken at an OATS facility to determine the impact of a fiberglass structure on emissions measurements being conducted within the building shown in Figure 91 [6]. The building is used to protect equipment and provide temperature stabilization during measurements. Measurements were taken using the 1.2 m TEM-horn antenna. This OATS facility was designed around the ANSI C63.7 standard, which provides qualitative guidelines concerning the type and construction of shelters, but does not provide and quantitative information on the effects of the shelter on the measurements. The measurements of this facility were performed with a time-domain measurement system to quantify shelter effects.

The OATS facility was designed to be both a Type-1 and a Type-2 structure. A Type-1 structure encloses the measurement range including the equipment under test and the transmitting and receiving antennas, which are placed 3 m apart. Type-2 facilities enclose only the equipment under test, and the receiving antenna is placed 10 m down range. The measurements discussed in



Figure 91. Evaluation of OATS facility using 1.2 m TEM horn antennas.

the technical note will be the Type-2 results. A brief summary of the Type-1 results is presented, but for further details refer to the paper [6].

Again the measurement sequence is as follows: (1) a reference measurement is taken; with the TEM horn antennas placed at a height of 1.6 m and a separation distance of 10 m on an unobstructed area of the OATS; (2) the receiving antenna is then placed 10 m down range of the shelter and the transmitting antenna is placed inside the shelter to obtain the shelter measurement; (3) the two spectra are then time-gated in the time-domain and transformed back into the frequency domain to obtain the shelter effects. The equation governing this quantity is

$$\Delta = \frac{|S_{12g}(\text{shelter})|}{|S_{12g}(\text{reference})|}, \quad (8)$$

where  $\Delta$  represents the deviation in site attenuation due to the presence of the shelter,  $S_{12g}(\text{shelter})$  and  $S_{12g}(\text{reference})$  are the frequency-domain amplitude spectra of the shelter and reference, respectively. The time-domain waveforms associated with this measurement are shown in Figure 92. The amplitude differences seen between the two waveforms are due to the presence of the shelter. We see additional shelter scattering effects immediately after the direct path and ground bounce signatures. The results showed that the shelter is not electrically

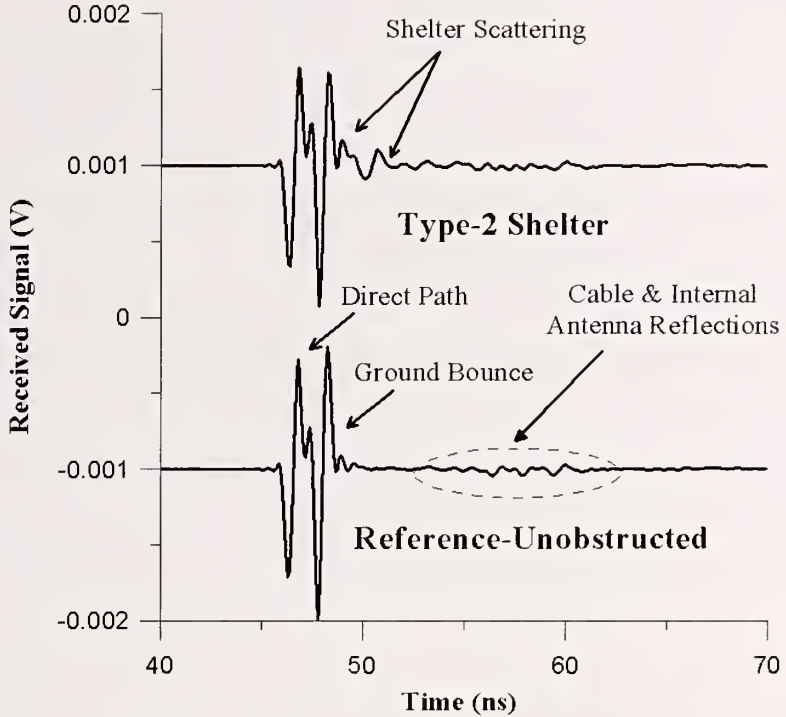


Figure 92. Time-domain transmission results for the reference and shelter measurements. The antennas were oriented in the vertical polarization.

transparent in the frequency range from 30 MHz to 1200 MHz. In the Type-1 measurements, the antennas were aligned along the short and long dimensions of the shelter, and the results showed that the shelter effects were significantly reduced with the antennas both inside. Moreover, the observed deviations seen in the long direction of the shelter were likely due to scattering from the structural beams. In summary, the shelter has a large effect on the measurement, and our time-domain system can distinguish between scattering events, which can prove useful in understanding data taken at such sites.

#### **4.5 EMC Compliance Chamber Testing**

The short-impulse response of TEM horn antennas makes them a powerful tool for testing EMC facilities [34]. TEM horn antennas were used in a portable measurement system to determine whether modifications to an EMC chamber were successful, or whether further improvements were required. The measurement frequency range of the system is from 30 MHz to 1200 MHz, the bandwidth of the 1.2 m TEM horn antennas.

Industry is increasingly required to improve both accuracy and efficiency of emissions and immunity testing procedures. For this reason, the NIST time-domain system was used to

evaluate an absorber-lined chamber. The NIST system has the following positive characteristics: (1) it lessens the need for site-to-site comparisons, (2) it provides the ability to observe directly changes to chamber, (3) it uses time-gated reference to minimize cost and time of quasi free-space reference, (4) it has high range resolution capabilities, and (5) it reduces chamber-antenna coupling. The system is the same as previously mentioned in Sections 4.3 and 4.4, so attention will be focused on the data-processing method in this section.

The intent of the data-processing sequence is to isolate the desired propagation effects and then to use these to determine two separate measurement metrics. The first metric is M1, which defines the response of the entire chamber and reveals imperfections in the chamber environment. The second metric is M2, which time-gates out the direct antenna coupling and allows us to define the scattering from the chamber boundary.

The data processing sequence is as follows and is shown in Figure 93:

- (1) Continuous-wave (cw) transmission data taken using a VNA,
- (2) Inverse Fourier transform applied,
- (3) Time-gate 1 applied or Time-gate 2 applied,
- (4) Fourier transform applied,
- (5) Performance metrics M1 and M2 obtained.

Time-domain results are shown in Figure 94. Details of the measurements before and after the retrofit are described in [35], as well as the pertinent equations and results of the testing. These antennas are important for other EMC applications [34 – 37] such as compliance, immunity testing, and radiated emissions, and have excellent antenna characteristics for such measurement applications.

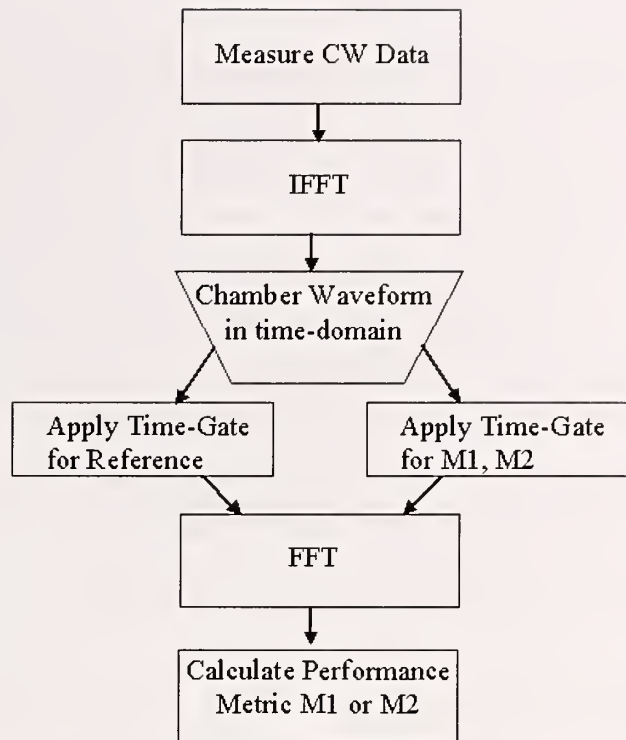


Figure 93. Signal-processing sequence.

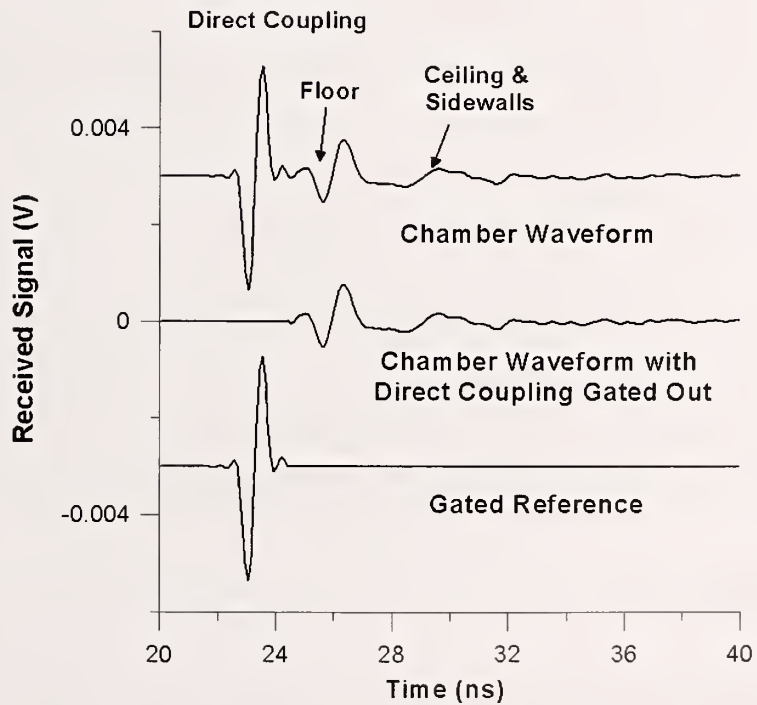


Figure 94. Various gating techniques to obtain chamber performance metrics, M1 and M2.

## ***4.6 Conducted and Radiated UWB Emissions***

These important ultrawideband (UWB) emissions measurements will be very briefly discussed here; for details refer to reference [38]. These tests were used to measure emissions from common UWB devices in order to determine the interference probability. This system consisted of a single-event transient digitizer and the 36 cm TEM full-horn antennas as receiving antennas. Signal processing techniques, similar to previous sections, are used to obtain the resultant spectral amplitude characteristics, which can then be used to determine suspect frequencies. The importance of using TEM horn antennas in these measurements is to allow us to resolve the impulse characteristics of these devices and to minimize the influence that the receiving characteristics of the antenna has on the device under test.

## ***5. Conclusions***

We have presented design equations, numerical modeling, and insight on constructing three ultrawideband, phase-linear, short-impulse response TEM horn antennas. The 1.2 m TEM horn antenna covers the frequency band from 30 MHz to 1.5 GHz. The 36 cm TEM full-horn antenna covers the frequency band from 100 MHz to 4 GHz. The 36 cm TEM half-horn antenna is appropriate for ground-plane based measurements. The balun design and resistive taper design are important for proper impedance matching, and each design is unique to the antenna, although standardization is possible. Pattern measurements and design modifications have been simulated in a finite-element modeling environment and have provided insight into measurements and pattern behavior. Finally, various applications were presented showing how these antennas are employed in aircraft shielding measurements, compliance chamber testing, facility evaluations, and free-space material measurements. Because of the favorable characteristics of these types of antennas, we are able to measure in a wide variety of measurement environments.

## ***6. Acknowledgments***

We enthusiastically applaud the career-long research of Arthur Ondrejka, who has dedicated his efforts to the pursuit of the perfect TEM horn antenna. Without his valuable insights, our research would not be where it is today. We also thank John Ladbury, who has done much of the initial research and measurements along with Mr. Ondrejka. Finally, we thank James

Baker-Jarvis, Office of Law Enforcement Standards (OLES), and the Department of Homeland Security for funding the materials measurements discussed in Section 4.1.

## 7. *References*

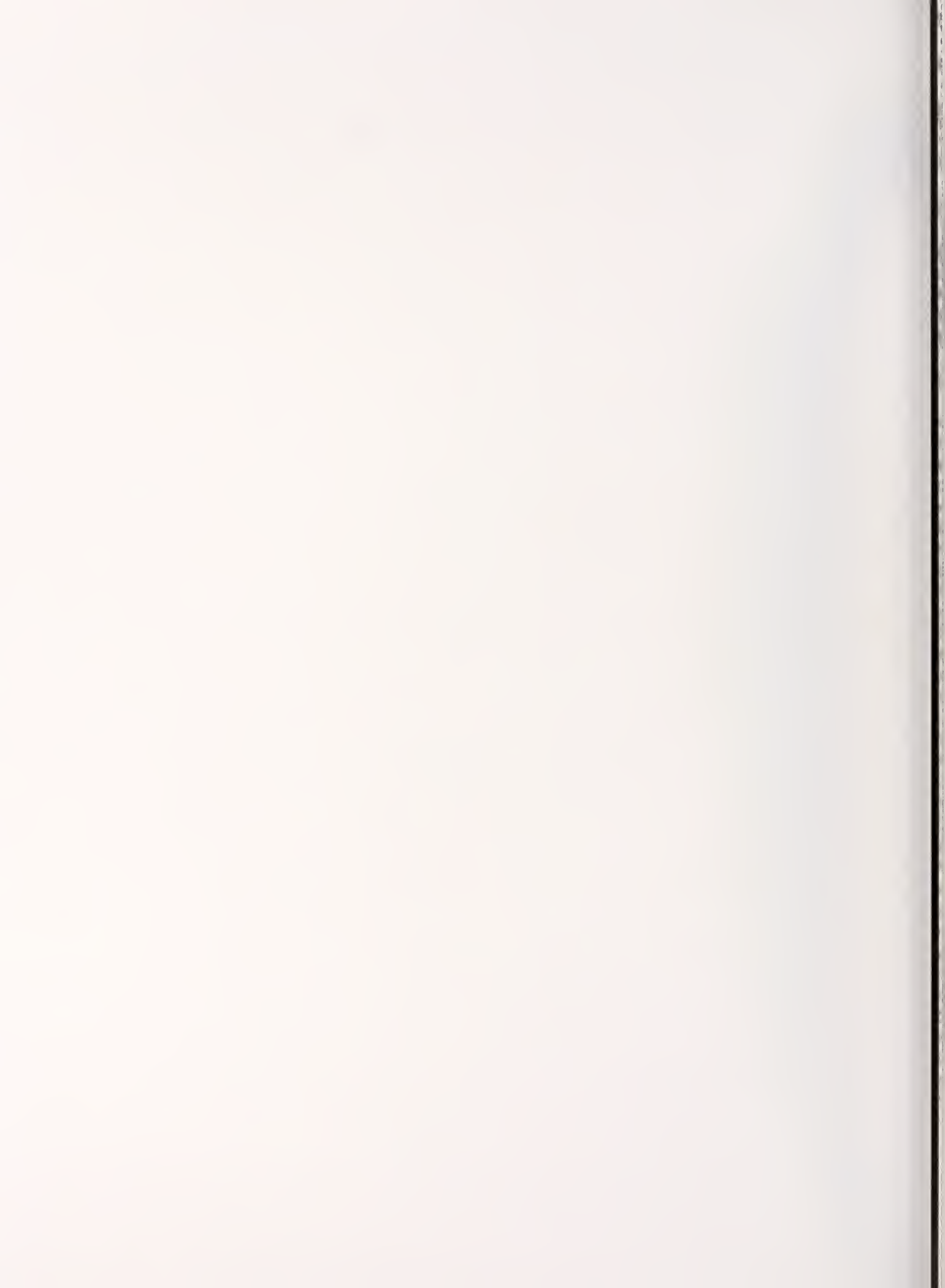
- [1] R. A. Lawton, A. R. Ondrejka. Antennas and the associated time-domain range for the measurement of impulsive fields. Nat. Bur. Stand. (U.S.) Technical Note 1008 (November 1978).
- [2] O. Allen, D. A. Hill, A. J. Ondrejka, Time-domain antenna characterizations. IEEE Trans. Electromagn. Compat. 35(3): 339-346 (August 1993).
- [3] R. T. Lee, G. S. Smith, A design study for the basic TEM horn antenna, IEEE Antennas Propagat. 46(1): 86-92 (February 2004).
- [4] K. Chung, S. Pyun, S. Chung, J. Choi, Design of a wideband TEM horn antenna. 2003 IEEE Intl. Symp. on AP 1: 229-232 (June 2003).
- [5] R. T. Johnk, D. R. Novotny, C. M. Weil, M. Taylor, T. L. O'Hara, Efficient and accurate testing of an EMC compliance chamber using an ultra-wideband measurement system. 2001 IEEE Intl. Symp. on Electromagnetic Compatibility 1: 302-307 (August 2001).
- [6] R. T. Johnk, D. R. Novotny, C. M. Weil, H. W. Medley, Assessing the effects of an OATS shelter: Is ANSI C63.7 enough? 2000 IEEE Intl. Symp. on Electromagnetic Compatibility 2: 523-528 (August 2000).
- [7] D. R. Novotny, R. T. Johnk, C. A. Grosvenor, N. Canales, Panoramic, ultra-wideband diagnostic imaging of test volumes. 2004 IEEE Intl. Symp. on Electromagnetic Compatibility 1: 25-28 (August 2004).
- [8] G. J. Freyer, M. O. Hatfield, T. A. Loughry, R. Johnk, D. M. Johnson, Shielding effectiveness measurements for a large commercial aircraft. 1995 IEEE Int. Symp. on Electromagnetic Compatibility, 383-386 (August 1995).
- [9] C. A. Grosvenor, R. T. Johnk, D. R. Novotny, N. Canales, C. M. Weil, J. Veneman, A two-phase airframe shielding performance study using ultra-wideband measurement systems. Natl. Inst. Stand. Tech. NISTIR 6622 (January 2003).
- [10] M. Kanda, The time domain characteristics of a traveling-wave linear antenna with linear and non-linear loads. Nat. Bur. Stand. (U.S.) NBSIR 78-892 (February 1979).
- [11] E. K. Miller, Editor, Time-domain measurements in electromagnetics. New York: Van Nostrand Reinhold Co. (1986).
- [12] M. Kanda, Time domain sensors and radiators. Chapter 5, New York: Van Nostrand Reinhold Co. (1986).

- [13] K. L. Shlager, G. S. Smith, J. G. Maloney, Accurate analysis of TEM horn antennas for pulse radiation. *IEEE Trans. Electromagn. Compat.* 38(3): 414-423 (August 1996).
- [14] R. T. Lee, G. S. Smith, On the characteristic impedance of the TEM horn antenna. *IEEE Trans. Antennas Propagat.* 52(1): 315-318 (January 2004).
- [15] F. M. Greene, Development of electric and magnetic near-field probes. *Nat. Bur. Stand. (U.S.) Tech Note* 658 (January 1975).
- [16] M. Kanda, The characteristics of broadband, isotropic electric field and magnetic field probes, *Nat. Bur. Stand. (U.S.) NBSIR* 77-868 (November 1977).
- [17] G. Franceschetti, C. H. Papas, Pulsed antennas. *IEEE Trans. Antennas Propagat.* AP-22(5): 651- 661 (September 1974).
- [18] A.R.A. Technologies. Inc. [web page] 2004: [http://www.aratech-inc.com/\\_private/Antennas.htm](http://www.aratech-inc.com/_private/Antennas.htm) [Accessed 8 March 2004].
- [19] K. C. Gupta, R. Garg, I. Bahl, P. Bhartia. *Microstrip lines and slotlines*. Artech House, Inc., Second ed. p. 10 (1996).
- [20] F. E. Gardiol, *Microstrip circuits*. New York: Wiley (1994).
- [21] F. Assadourian, E. Rimai, Simplified theory of microstrip transmission systems. *Proc., Inst. Radio Eng.* 40: 1651-1657 (December 1952).
- [22] Website: M/A COM, Inc. [web page] 2006; <http://www.macom.com/DataSheets/TP-103.pdf> [Accessed 25 May 2006].
- [23] Website: Sirenza Microdevices, Inc. [web page] 2006; <http://www.sirenza.com/pdfs/datasheets/FP-522.pdf> [ Accessed 25 May 2006].
- [24] M. Kanda, The effects of resistive loading on TEM horns. *Nat. Bur. Stand. (U.S.) NBSIR* 79-1601 (August 1979).
- [25] S. Evans, F. N. Kong, TEM horn antenna: Input reflection characteristics in transmission. *Proc., IEE 130H(6)*: 403-409 (October 1983).
- [26] L. T. Chang, W. D. Burnside, An ultrawide-bandwidth tapered resistive TEM horn antenna. *IEEE Trans. Antennas Propagat.* 48(12): 1848-1857 (December 2000).
- [27] A. Sinopoli, W. D. Burnside, A slotline/bowtie hybrid antenna for use as a compact range feed. *Ohio State Univ. Tech. Report* 7219, 29-46 (March 1992).
- [28] C. Kyungho, S. Pyun, C. Jaehoon, Design of an ultrawide-band TEM horn antenna with a microstrip-type balun. *IEEE Trans. Antennas Propagat.* 53(10): 3410-3413 (October 2005).

- [29] E. B. Larsen, R. L. Ehret, D. G. Camell, G. H. Koepke. Calibration of antenna factor at a ground screen field site using an automatic network analyzer. 1989 IEEE Symp. on Electromagnetic Compatibility, pp. 19-24 (May 1989).
- [30] J. G. Veneman, D. R., Novotny, C. A. Grosvenor, R. T. Johnk, N. Canales, Ultra-wideband antenna pattern characterization in a non-ideal EM facility. Antenna Measurement Techniques Association 24<sup>th</sup> Annual Mtg. and Symp. pp. 96-100 (November 2003).
- [31] J. Baker-Jarvis, M. D. Janezic, J. H. Grosvenor, R. G. Geyer. Transmission/reflection and short-circuit line methods for measuring permittivity and permeability. Natl. Inst. Stand. Technol. Tech. Note 1355 (1992).
- [32] R. T. Johnk, C. A. Grosvenor, D. G. Camell, D. R. Novotny, Ultrawideband shielding evaluation of a business jet. SAE AE-2 Lightning Committee, Portland, ME, May 16-18, 2006.
- [33] D. R. Novotny, R. T. Johnk, A. Ondrejka, Analyzing broadband, free-field, absorber measurements. 2001 IEEE Intl. Symp. on Electromagnetic Compatibility 2: 1152-1157 (August 2001).
- [34] M. J. Alexander, EMC antenna considerations. Compliance Eng. (July-August 2003).
- [35] M. J. Alexander, Using antennas to measure the strength of electric fields near equipment. Compliance Engineering Annual Reference Guide 17(3): 66-83 (2000).
- [36] K. Armstrong, T. Williams, EMC testing, Part 1: Radiated emissions. EMC Compliance J. 27-39 (February 2001).
- [37] C. A. Grosvenor, R. Johnk, D. Novotny, N. Canales, TEM-horn antennas: A promising new technology for compliance testing. Intl. Symp. on Electromagnetic Compatibility 1: 25-28 (9-13 August 2004).
- [38] R. T. Johnk, D.R. Novotny, C. A. Grosvenor, N. Canales, J. G. Veneman, Time-Domain measurements of radiated and conducted ultra-wideband emissions. 2003 IEEE Conf. on Ultra Wideband Systems and Technologies 245-249 (November 2003).







# *NIST Technical Publications*

## *Periodical*

**Journal of Research of the National Institute of Standards and Technology**—Reports NIST research and development in metrology and related fields of physical science, engineering, applied mathematics, statistics, biotechnology, and information technology. Papers cover a broad range of subjects, with major emphasis on measurement methodology and the basic technology underlying standardization. Also included from time to time are survey articles on topics closely related to the Institute's technical and scientific programs. Issued six times a year.

## *Nonperiodicals*

**Monographs**—Major contributions to the technical literature on various subjects related to the Institute's scientific and technical activities.

**Handbooks**—Recommended codes of engineering and industrial practice (including safety codes) developed in cooperation with interested industries, professional organizations, and regulatory bodies.

**Special Publications**—Include proceedings of conferences sponsored by NIST, NIST annual reports, and other special publications appropriate to this grouping such as wall charts, pocket cards, and bibliographies.

**National Standard Reference Data Series**—Provides quantitative data on the physical and chemical properties of materials, compiled from the world's literature and critically evaluated. Developed under a worldwide program coordinated by NIST under the authority of the National Standard Data Act (Public Law 90-396). NOTE: The Journal of Physical and Chemical Reference Data (JPCRD) is published bimonthly for NIST by the American Institute of Physics (AIP). Subscription orders and renewals are available from AIP, P.O. Box 503284, St. Louis, MO 63150-3284.

**Building Science Series**—Disseminates technical information developed at the Institute on building materials, components, systems, and whole structures. The series presents research results, test methods, and performance criteria related to the structural and environmental functions and the durability and safety characteristics of building elements and systems.

**Technical Notes**—Studies or reports which are complete in themselves but restrictive in their treatment of a subject. Analogous to monographs but not so comprehensive in scope or definitive in treatment of the subject area. Often serve as a vehicle for final reports of work performed at NIST under the sponsorship of other government agencies.

**Voluntary Product Standards**—Developed under procedures published by the Department of Commerce in Part 10, Title 15, of the Code of Federal Regulations. The standards establish nationally recognized requirements for products, and provide all concerned interests with a basis for common understanding of the characteristics of the products. NIST administers this program in support of the efforts of private-sector standardizing organizations.

*Order the following NIST publications—FIPS and NISTIRs—from the National Technical Information Service, Springfield, VA 22161.*

**Federal Information Processing Standards Publications (FIPS PUB)**—Publications in this series collectively constitute the Federal Information Processing Standards Register. The Register serves as the official source of information in the Federal Government regarding standards issued by NIST pursuant to the Federal Property and Administrative Services Act of 1949 as amended, Public Law 89-306 (79 Stat. 1127), and as implemented by Executive Order 11717 (38 FR 12315, dated May 11, 1973) and Part 6 of Title 15 CFR (Code of Federal Regulations).

**NIST Interagency or Internal Reports (NISTIR)**—The series includes interim or final reports on work performed by NIST for outside sponsors (both government and nongovernment). In general, initial distribution is handled by the sponsor; public distribution is handled by sales through the National Technical Information Service, Springfield, VA 22161, in hard copy, electronic media, or microfiche form. NISTIRs may also report results of NIST projects of transitory or limited interest, including those that will be published subsequently in more comprehensive form.

**U.S. Department of Commerce**  
National Bureau of Standards and Technology  
325 Broadway  
Boulder, CO 80305-3328

**Official Business**  
Penalty for Private Use \$300